IMPACT: A Facility for Studying the Interaction of Low-Energy Intense Charged Particle Beams with Dynamic Heterogeneous Surfaces

J. P. Allain,[a] M. Nieto, M. R. Hendricks, P. Plotkin, S. S. Harilal, A. Hassanein
Mathematics and Computer Science Division
Argonne National Laboratory, 9700 S. Cass Avenue, Argonne, IL 60439

The Interaction of Materials with Particles and Components Testing (IMPACT) experimental facility is furnished with multiple ion sources and in situ diagnostics to study the modification of surfaces undergoing physical, chemical, and electronic changes during exposure to particle beams. Ion beams with energies in the range of 20 to 5000 eV can bombard samples at flux levels in the range of 10^{10} to 10^{15} cm^{-2} s^{-1}; parameters such as ion angle of incidence and exposed area are also controllable during the experiment. IMPACT has diagnostics that allow full characterization of the beam, including a Faraday cup, a beam imaging system, and a retarding field energy analyzer. IMPACT is equipped with multiple diagnostics, such as electron (Auger, photoelectron) and ion scattering spectroscopies, that allow different probing depths of the sample to monitor compositional changes in multicomponent or layered targets. A unique real-time erosion diagnostic based on a dual quartz crystal microbalance measures deposition rates smaller that 0.01 nm/s, which can be converted to sputter yields given a particular crystal position and sputtered angular distribution. The monitoring crystal can be rotated and placed in the target position in order to probe the quartz crystal oscillator surface without having to transfer it outside the chamber.

Keywords: sputtering, in situ metrology, ion scattering spectroscopy, ion sources, electron spectroscopy erosion rate, EUV reflectometry

PACS: 33.60.Fy, 34.50.Dy, 34.80.i, 61.10.ky

[a] Author to whom correspondence should be addressed. Electronic mail: allain@anl.gov

I. INTRODUCTION

The study of surfaces and interfaces and their interaction with energetic particles during thin-film growth and nanostructure fabrication has inspired the design of advanced in situ characterization experiments and experimental facilities.[1-3] In addition, designing experiments that simulate complex environments (e.g., particle irradiation of multicomponent surfaces) and the ability to diagnose individual mechanisms and properties has become vital for computational modeling benchmarking.[4-6] Computational codes have become critical in complementing and extending understanding of the fundamental processes during synthesis of nanoscale structures and ultra-thin film systems.

Tailoring functional and dynamic properties of future nanoscale devices and systems requires knowledge of how these properties behave on both broad temporal and spatial scales. Heterogeneous thin-film growth and synthesis of advanced materials using energetic particle bombardment also requires insight of the elemental, chemical, and structural state evolution during particle irradiation. The low-dimensional states inherent in nanostructure systems at a surface (i.e., metal clusters, nanostructure island coalescence, interface modification) demand a set of complementary surface-sensitive characterization tools able to resolve a complex set of variables in space and time. For example, hyperthermal (500–1000 eV) Sn ions are an ultra-shallow implant in Ru thin-film mirrors penetrating a few monolayers (1–2 nm) below the air/film interface. The implanted species affect the optical reflective properties of the mirror at wavelengths that approach the implantation zone. This phenomenon is important in 13.5 nm extreme ultraviolet lithography (EUV) for future nanometer-scale feature sizes.[7-11]

In another application, surfaces and interfaces of thin films used in the fabrication of advanced nonvolatile memories require the use of sophisticated characterization systems able to

adequately diagnose chemical, kinetic, and thermodynamic behavior of the thin films and the materials integration strategies required for the development of next-generation devices. These capabilities are particularly important when characterizing ultra-thin interfacial zones relevant to the compatibility and performance of ultra-thin dielectric materials for next-generation complementary metal-oxide-semiconductor (CMOS) devices.[1]

The Interaction of Materials with Particles and Components Testing (IMPACT) experimental facility has been designed for studies of in situ dynamic heterogeneous surfaces at the nanoscale exposed to varied environments that modify surface and interface properties. The philosophy behind experiments in IMPACT relies heavily on its ability to provide a wide array of characterization techniques and conditions that properly simulate complex environments. The IMPACT facility achieves this by atomic-scale characterization of the evolution of elemental, chemical, and thermodynamic states of ultra-thin film surface and interfaces using complementary surface-sensitive characterization techniques**.** In situ techniques used in the IMPACT experiment include low-energy ion scattering spectroscopy (LEISS) with simultaneous forward and backward scattering modes, direct recoil spectroscopy (to study impurity levels in the film), x-ray photoelectron spectroscopy (XPS), Auger electron spectroscopy (AES), EUV (13.5 nm) reflectometry (EUVR), extreme ultraviolet photoelectron spectroscopy (EUPS), and mass spectrometry using both quadrupole and magnetic sector analyzers. EUPS combined with LEISS can give chemical state and elemental information at the first 2-3 monolayers (MLs), respectively. AES and XPS give similar information at probing depths from two to three monolayers down to about 10–15 nm into the bulk of a thin film.

Both ion and electron spectroscopies are conducted by using a highly sensitive hemispherical sector energy multichannel analyzer. High-resolution depth profiles are obtained

by using a unique low-energy ion source delivering 100 eV ions of any desired inert gas species at current densities of 2.5 $\mu A/cm^2$. Simultaneous with surface analysis of the irradiated sample, the total erosion flux is measured in situ by using an ultra-sensitive temperature-compensating quartz crystal nanobalance–dual crystal unit (QCN-DCU) with resolution better than 0.005 Å/sec. During ion etching the sample can be tilted at any desired angle with respect to its surface normal from 0° to 60°, with a resolution of better than 0.1°. Dynamic effects induced by energetic charge particles can range from induced surface morphology evolution to physical sputtering. IMPACT is designed to primarily study the effects of the latter by means of mass loss techniques.

This paper is organized in the following manner. Section II describes auxiliary systems for the IMPACT facility. Included is a description of the various ion sources and ion-beam diagnostics, the IMPACT photon sources, the evaporation system and its calibration, and the hemispherical energy sector analyzer and QCM-DCU. Section III presents details of the surface analytical techniques used in IMPACT. Section IV discusses results of a "model" experiment and concludes with a short summary of IMPACT capabilities.

II. IMPACT EXPERIMENTAL FACILITY

A. Chamber and Target Delivery

The basic experimental setup is made up of key auxiliary systems. Auxiliary systems in IMPACT consist of three major components: the vacuum system, the sample transfer system, and the gas delivery system.

One of the most vital components of the IMPACT experimental facility is the design of the vacuum chamber, custom-made to provide functionality and versatility. **Figure 1** shows the

schematic of the main vacuum chamber with various radiation/particle sources and diagnostic tools. The IMPACT vacuum chamber is equipped with 55 ports, each designated for a particular application. The vacuum system consists of two oil-less scroll pumps, a turbomolecular pump, and an ion pump. Ion sources and supplementary chambers (i.e., load-locks, transfer chambers, preparatory chambers) are differentially pumped. The ultimate pressure achieved with just the roughing pump is of a few microbars, and the rate of rise in the chamber is typically less than 0.5 μbar/min. Once the ultimate pressure of the rough pump is reached, the gate valve to an oil-less Leybold magnetically levitated turbomolecular pump is opened, and the chamber is taken to an ultimate pressure of less than 1 nbar in a few hours. If the vacuum chamber has been vented for an extended period of time or exposed to a humid environment, an internal halogen lamp is used to help eliminate adsorbed water on internal chamber surfaces. Once the pressure is less than 1 nbar, a gate valve is opened to the ion pump. The GV TiTan ion pump is a 350 l/s system equipped with Ti sublimation elements that increase the pumping efficiency. With the ion pump open, IMPACT reaches the lowest attainable pressure, around 0.001 nbar. The partial pressures of the background gases in the chamber during the experiments are monitored with a mass spectrometer.

The sample transfer system in IMPACT allows higher sample throughput, since venting of the system is avoided. Samples are placed in sample platens especially constructed to fit on the platen holder inside IMPACT. The platen is placed in a small chamber with a quick-vent door, sitting on top of a fork-shaped holder mounted at the end of a long (2-meter) magnetically coupled linear travel arm. Once the sample is in the fork holder, the small chamber is evacuated by using a turbopump. When the pressure in the load-lock chamber is less than 1 nbar, an opening between the load-lock chamber and the IMPACT chamber is created by a gate valve,

and the fork holder is inserted. Since the travel arm is mounted on a pivoting base, the travel arm can flex up and down with high precision by means of a screw and a custom-engineered hinge. After the platen with the sample is placed in the platen holder inside IMPACT, the travel arm is retracted, and the opening between the load-lock chamber and the IMPACT chamber is closed. In order to extract a sample, the process is repeated in reverse. Up to four samples can also be stored inside the main chamber for cases of multiple-sample analysis. The gas delivery system in IMPACT injects high-purity gases (> 99.999% purity) to the differentially pumped ion sources via a manually controlled valve.

B. Ion Sources

The charged-particle beam sources in IMPACT play a key role both as excitation/probing sources (i.e., secondary electron emission, ion scattering spectroscopy) and as modifying sources (i.e., implantation, ion-induced desorption, etching). They also provide a means to simulate conditions found in prototype devices such as plasma processing devices or fusion reactor systems. Currently IMPACT has four specialized sources, each with a specific function and a unique capability. All the ion sources currently installed are hot filament sources except for one based on thermionic emission. The following subsections describe each ion source with both its capability and its application.

1. High-Energy Ion Source

An NTI 1401 ion source installed in IMPACT is capable of operating with all noble gases and a few reactive gases, including hydrogen, nitrogen, and oxygen. Its multiple optical elements allow full control over the beam spot size, as well as a long working distance, so that submillimeter beam spots can be obtained 10 cm from the source exit. Four levels of electron

emission can be achieved, resulting in control over the incident ion flux on surfaces. An octopole ion optics element at the ion-gun shaft exit provides rastering capabilities that result in flexibility in the size of area exposed to the beam and consequently a secondary control of the ion flux. Ion fluxes in the range 10^{10}–10^{15} cm^{-2} s^{-1} are routinely achieved. The ion energy range for this source is between 100 eV and 5 keV, although lower energies are possible at the cost of both current and beam size. The dependence of the NTI 1401 ion source current on ion energy is plotted in **Fig. 2** and compared to another ion source summarized below. The NTI 1401 ion source is used mostly as a diagnostic tool for low-energy ion scattering spectroscopy. The ion source is also used for sample cleaning when other methods are not sufficient or available.

2. Low-Energy Ion Source

The NTI 1402 ion source installed in IMPACT is a specialized low-energy ion source, similar in design to the 1401, but with modified optics to allow ion extraction at lower energies, even below 100 eV. The spot size and current can be controlled by the user; but because of the nature of the extraction process, the maximum flux is reduced to about 10^{14} cm^{-2} s^{-1} for ion beams with energies below about 80–90 eV, as shown in **Fig. 2**. To assess the energy spread of the low-energy ion source, we measured it with a retarding field analyzer (RFA, details of which are given in Subsection II.5). The data for three energies (50, 100, and 150 eV) of a singly charged Ar^+ beam is shown in **Fig. 3**. The plot shows the negative derivative of the normalized current vs applied voltage data for each of the incident energies. The energy spread is 3.8%, 4.9%, and 5.7% for 50, 100, and 150 eV, respectively, with a Gaussian centroid shift no more than 3.0 eV from the applied voltage of the ion source. As the ion beam energy decreases, the size of the beam starts to increase because of Coulomb repulsion, as illustrated in **Fig. 4**, which

shows the spatial profile of ion beams with different impact energies. The measurement is conducted by moving the RFA manipulator arm linearly with a resolution of 0.05 mm.

3. Metal Ion Source

The 14MS ion source is a metal ion source currently operated with Sn but upgradable to metals with relatively low vapor pressures. A slug of the metal is heated inside the gun ionizer, and some metal ions are generated. The gun is designed so that operation with gaseous species is also possible. In addition to an optical column similar to the other ion sources, the 14MS is equipped with a Wein filter with a 3° bend, which filters particles with a particular mass to charge ratio to exit the gun. The separation is done by varying the current on the filter's electromagnet, enabling the selection of the mass or charge state of the ion. When the 14MS NTI source is operated with metal ions, its primary function is that of implantation and near-surface modification. Typical operational energies used with Sn ions range from 500 eV to 2000 eV, depending on the particular experiment. An example of its use in exposure of metal thin-films is given in Section IV.

4. Lithium Ion Source

Another source installed in IMPACT is a Li ion source. Unlike all the previous ones, this source does not operate with gas, only with its internal Li charge. The reason is that the main principle for ion generation is via the thermionic process. A lithium-impregnated ceramic surface is heated to very high temperatures, thus emitting Li atoms in the ionic charge state. Fluxes up to 10^{14} cm^{-2} s^{-1} in the energy range 500–5000 eV can be achieved with this source.

The Li alkali metal source is used for two applications in IMPACT. In the first application, Li ions are used as an implanting species during simulated experiments of tokamak

plasma-facing surfaces. Recent studies have focused on the use of lithium as a plasma-facing component (PFC) in tokamak plasmas, and thus interest exists for measurement of fusion candidate materials under Li-ion bombardment simulating redeposition of sputtered Li particles.[12] In the second application, Li ions are used for low-energy ion scattering for structural analysis of metal surfaces. This application is possible because of the relatively high probability of ionization of Li atoms scattering from metal surfaces. Thus, unlike scattered particles of inert gas, Li ions scattered from surfaces can give information from subsurface atoms (below 2–3 ML) thus yielding structure details.[13]

5. Ion Beam Diagnostics

Since ion beams are critical for performing studies in the IMPACT facility, it is imperative to have adequate diagnostics that measure ion beam parameters such as size, intensity, and energy. Various diagnostics are used in the characterization of ion beams in IMPACT. The diagnostics consist of a partially oxidized alkali-metal screen, a 5-pinhole Faraday cup, and an RFA. Each diagnostic has distinct functions, and each is used for particular calibration tests prior to performing experimental runs in IMPACT.

The lithium diagnostic takes advantage of the 671 nm LiI line emission, excited when incident energetic inert gas ions collide with surface Li atoms. The emitted light is an indirect measurement of the size of the ion beam and a direct measurement of its location. This diagnostic is used mainly for positioning the beam and measuring the general beam raster areas, allowing a rough estimate of the ion flux in combination with the ion-beam current measured in series with a pico-ammeter. The alkali-metal screen cannot be used for beams with less than 200 eV of energy or for ion-beam currents less than 50 nA because the light emission is too low to be detected by a CCD camera.

A more sophisticated diagnostic that measures is a five-pinhole Faraday cup, which measures the beam size and current. This instrument's primary disadvantage is the time required for setup during calibration tests. This diagnostic is therefore performed only once for calibration purposes for a collection of experiments under similar ion-exposure conditions. Five pinholes are arranged at known distances between them, and a collector plate sits behind the pinholes. The beam is rastered on top of the plate, and the beam size is calculated by knowing the displacement of the beam over the pinhole, determined from a scan over the whole plate that shows the position of the pinholes. **Figure 5** shows a sample beam profile of 1 keV He^+ obtained with this method. One advantage of this instrument is generation of two-dimensional spatial profiles; however, it is limited to profiling of beams smaller than 3 mm in diameter.

The diagnostics described above can be used to measure the size of the ion beam and its location, but this measurement gives no information about the energy distribution of the beam. Determining whether the ion source energy peaks at the value specified by the controller setting during operation is very important, in particular for applications that rely on low-energy ion-induced surface studies. In addition, any significant energy spread can influence the spectral response during ion scattering, thus introducing uncertainty in mass identification. In order to perform energy distribution measurements, a retarding field analyzer (RFA) similar to the type used by Jacob et al. [2] was constructed, as shown in **Fig. 6.** The RFA consists of a grounded metal tube containing two grids and a plate, all electrically isolated from its housing. A metal plate with a hole, also isolated from the body, covers the entrance to the RFA. The diagnostic is mounted on a linear manipulator with 0.05 mm resolution, so it can be used to profile the beam without having to raster it, as is the case for the pinhole Faraday cup. The beam is aligned so that the current read in the top plate is minimized and the current in the collector plate at the bottom

of the RFA is maximized. Once these conditions are met, the RFA is moved either in or out, and the current on the collector is recorded as a function of distance from the maximum current position; this procedure allows the calculation of the beam in one dimension. In order to measure the energy distribution of the beam, the top plate and the top grid of the RFA are grounded. The bottom grid is biased with a voltage between 0 and a value 1.1 times the nominal beam energy (in eV). The collector plate records the current as a function of bias voltage; and by taking the derivative of this data, the energy spread of the beam can be calculated. **Figure 7** shows the measurements for 150 eV argon and xenon ion beams.

C. Photon Sources

1. X-Ray Source

IMPACT has a dual-anode (Mg and Al), actively cooled x-ray source used to perform XPS studies. The main advantage of using a dual anode is that the presence of two different excitation energies enables rapid distinction of Auger electron lines from photoelectron structures in an XPS spectrum. The Mg and Al anodes in the x-ray source produce radiation lines at 1253.6 eV and 1486.6 eV, respectively. A flux of 10^{11}–10^{12} photons/s emanates from the source, which translates into a photocurrent of 40–50 nA, depending on the material. The x-rays flood a circular area of about 1–2 cm^2. The footprint of the x-ray beam can be changed by modifying the working distance, since the source is mounted on a z-manipulator. The source can be retracted when it is not in use. The natural line-width of the radiation is lower than 1 eV, which is sufficient for XPS to determine binding energies of core levels within 0.2 eV.

2. EUV Source

Several systems in IMPACT rely on the use of soft x-ray sources. The two main systems are the EUV photoelectron spectroscopy system and the EUV reflectometry system; the latter is used more frequently than the former. The most important component of the EUV reflectometry and EUPS systems is the light source. Constraints regarding the space limitations and the ease of incorporation into the design were critical in selecting an adequate source. A Roentgen-type source with a silicon anode was used that emits radiation centered at 13.5 nm (92 eV).[14] The source has a steady power output of 10 μW/sr on the 13.5 ± 1 nm; however, the source opening limits the exit solid angle to 0.03 sr, so the net power output of the source is 250–300 nW. This power, assuming a mean energy of 92 eV, corresponds to a photon current of 10^{10} photons/s.

Since the EUV beam is not visible in the sample, the actual size of the EUV beam needs to be determined by using another method. The method chosen was to use a masked EUV reflecting sample, with one-fourth of the surface uncovered and the rest covered by a nonreflective material, in this case graphite. The sample is tilted to an angle expected to give non-zero reflection, between 46° and 48° and then is slowly retracted from the chamber. The distance that the sample is retracted is correlated to the location of the sample located at the chamber center, such that when the sample is fully inserted, the spot 3 mm past the center of the sample lies on the geometrical center of the chamber, where it is believed the EUV beam hits. The distance retracted can be correlated to the location with respect to the center of reflective region, as can be seen from **Fig. 8**. As the figure shows, the maximum reflectivity should occur when the sample is retracted 6 mm, since that corresponds to the EUV spot located halfway through the reflecting region (the zero in the lower scale of **Fig. 8**); if the maximum occurs at any other location, the EUV spot would not be located in the geometrical center of the chamber.

The results from the measurement are shown in **Fig. 9**, which has two sets of data. One set corresponds to the sample depicted in **Fig. 8** and is plotted with filled symbols. The other set is obtained by rotating the sample 90^{o} counterclockwise and repeating the measurements, in order to determine the symmetry with respect to the dotted line that bisects the sample in **Fig. 8.** If similar profiles are obtained in both configurations, the beam is symmetric with respect to that line.

From **Fig. 9** one can see that the maximum reflectivity is obtained between 6 mm and 8 mm. A Gaussian fit to the data reveals that the peak reflectivity occurs at 6.7 mm retracted for the reflective region in the upper left quadrant of the sample, and at 7.7 mm if the sample is in the lower left quadrant. The discrepancy of the results may be due to the angle of incidence of the light into the sample with respect to the motion axis, and also due to the elliptical shape of the EUV footprint on the sample. The beam size is calculated by taking one half of the Gaussian curves in Fig. 9 and taking the derivative, since the measurement is integral. The derivative plot is another Gaussian curve, and the full-width half-maximum of this curve is the actual size of the beam. The estimated spot-size diameter for the EUV light is 3 mm, but this size is not corrected for the elliptical shape of the footprint and the angle of incidence of the light with respect to the motion axis of the sample. Nevertheless, this measurement is sufficient to determine that the EUV light spot is small enough to be completely included in the areas of the sample that are modified during an experiment in IMPACT, which normally range from 0.25 cm^2 to 0.50 cm^2 rastered/exposed areas.

D. E-beam Evaporation Sources

A four-pocket electron-beam evaporator EGN-4 from Oxford Applied Research is installed in IMPACT to expose samples to a thermal source of particles. The e-beam evaporator is also used to deposit ultra-thin multilayer films. Currently, the evaporator is set to work with Sn and Li; however, up to four materials can be used at one time. The evaporator has also been custom designed to operate facing downward, which is particularly difficult for low-melting metals such as Sn and Li. Therefore, the custom design includes crucibles able to handle Sn and Li.

The evaporator is calibrated in two ways: in a separate chamber (ex situ) and in situ. The ex situ calibration uses a single quartz crystal microbalance (QCM), so the deposition rate of Sn, for example, can be measured for different power levels on the evaporator. The evaporator has current monitors near the exit of the crucible, which measure ion current between ground and the crucible or rod containing the evaporated material. This ion current is proportional to the evaporative flux by a constant factor that is material dependent. The procedure to calibrate the evaporator begins by setting the evaporator at a particular ion current (i.e., flux) level. The electron-beam evaporator is equipped with an in situ current monitor for closed-loop operation regulating the particle current from the evaporator. This is accomplished by sampling a small fraction of the vapor, which is intrinsically in an ionized state. Once the current is set, the mass gain of the crystal is monitored until a constant slope in the crystal frequency is established. This step is repeated for different current values, and a plot of the QCM frequency slope vs evaporator current is generated. The frequency slope to deposition rate is converted and divided by the film density to obtain the thermal flux.

Figure 10 shows the raw data from the QCM for Sn evaporation. Each slope on the graph corresponds to a current level of the evaporator. In order to convert from the frequency slope to deposition rate, the following formula is used:

$$\frac{dx}{dt} = \frac{166100\rho_{QCM}}{f_0^2 \rho_{evap}} \left(\frac{df}{dt} \right). \qquad (1)$$

Here, x is the deposited thickness (in nm), dx/dt is the deposition rate (in nm/s), ρ_{QCM} is the density of the QCM crystal, ρ_{evap} is the density of the deposited film, f_0 is the natural oscillation frequency of the QCM crystal, and df/dt is the slope of the QCM frequency response. This formula assumes that all evaporated flux is collected by the quartz crystal oscillator (QCO) and that the sticking probability is unity at the surface of the QCO. **Figure 10** can be transformed into a direct relationship between the deposition rate and the evaporator ion current using Eq. (1) because the current to the evaporator is known and the frequency response is measured. Since the relationship is linear with zero intercept, it is easy to relate the deposition rate to the evaporator current.

In order to avoid contamination of the chamber by vapor condensation, a conical nozzle was constructed to collimate the thermal flux, such that the deposition was confined to the sample area. After addition of the cone, the evaporated material is confined to the sample, and the deposition spot has a size of about 5–7 mm in diameter approximately centered on the sample. This area is calibrated for each experimental set and can vary in size within the sample boundaries. Because of the importance of calibrating the evaporation flux for each experiment, an in situ calibration scheme was installed. The IMPACT chamber was designed with a port whose centerline axis is perpendicular to the centerline axis of the EGN4 evaporator port. A manipulator arm was installed with a QCM system capable of measuring the deposition rate from

the EGN4 in situ and prior to each run. **Figure 11** shows the calibration result of the EGN4 current to deposition rate measured with the movable QCM in line with evaporator.

E. Hemispherical Energy Sector Analyzer

IMPACT uses a hemispherical energy sector analyzer (HESA), which performs energy separation on charged particles coming from the sample: electrons (AES, XPS, EUPS), scattered ions (LEISS), or charged recoils (DRS). Energy dispersion can be conducted for a kinetic energy range between 0 eV and 3500 eV by using a 150 mm diameter electrostatic hemispherical deflector. The analyzer has a drift tube with 10 electrostatic lenses and an iris located before the hemispherical capacitor (HC) entrance slit. Both entrance and exit slits are selectable as well; and after the HC exit slit, a five-channel electron multiplier (CEM) detector collects the energy-dispersed particles. Multiple lens modes are allowed, each suited for a different application. Magnification modes reduce the collection area to a small (0.2 x 0.2 mm) region to perform spatially resolved studies, point transmission for small excitation sources (such as focused ion and electron beams), and large collection area for measuring average contents over a large sample area. Energy resolution down to < 1 meV is possible with narrow energy dispersion, so the identification of elements and their chemical state is more reliable because of the high energy resolution of the analyzer, as it will be shown later in this paper. For ultra-high-energy resolution applications (e.g., EUPS) the retardation voltage can be operated in a 400 V or 40 V range with extremely low ripple, having an energy resolution down to 80–800 μeV with pass energies up to 200 eV.

The detection sensitivity for spectroscopic techniques in IMPACT is limited by the signal-to-noise ratio of the spectra obtained by the HESA detector. The area of a Gaussian peak with a given width d and maximum height H at the mean value is given by

$$A = \sqrt{2\pi} Hd \,. \tag{2}$$

If the width of the peak is a constant independent of the content, the uncertainty the area dA is correlated to the uncertainty in height H_{noise}:

$$dA = \sqrt{2\pi} dH_{noise} \,. \tag{3}$$

The atomic fraction of a particular component is given by

$$x_i = \frac{A_i / S_i}{\sum_{j=1}^{N} A_j / S_j} \,, \tag{4}$$

where A_i is the area of the peak corresponding to the i-th component, S_i is a sensitivity factor particular to component i, and the sum in the denominator is over the number of components N. The error in the fraction of component i due to the area error from all the components, assuming that all sensitivity factors are constant and that the noise H_{noise} is constant for all the components, is given by

$$\Delta x_i = \sqrt{2\pi} dH_{noise} \left[\sum_{j=1}^{N} \left(\frac{dx_i}{dA_j} \right)^2 \right]^{1/2} . \tag{5}$$

If the derivatives are written explicitly, the following expression is obtained for the error in the atomic fraction:

$$\Delta x_i = \frac{1}{\sum_{j=1}^{N} \frac{1}{S_j} \frac{H_{signal,j}}{H_{noise}}} \left[1 - 2x_i + x_i^2 \sum_{j=1}^{N} \left(\frac{S_i}{S_j} \right)^2 \right]^{1/2} . \tag{6}$$

Consider the case of a binary component system where one the peak corresponding to component 1 is 20 counts and the one corresponding to component 2 is 10,000 counts. Both peaks have a FWHM of 50, and the sensitivity factor for component 1 is 1 and for component 2 is 4. The noise of the system is 10 counts. The fraction of component 1 is then given by $x_1 = 0.008$. The error in the concentration for these particular values is 0.004, giving a relative error of about 50%, very close to the signal-to-noise ratio. For component 2, the relative error is about 2%, which is an order of magnitude higher than the ratio of noise to signal for that component.

Aside from the uncertainty issue already addressed, there is another issue associated with the minimum content of a component that can be detected, specifically, with the areal density of the component in the surface of the sample. Consider a surface composed of two atoms A and B, with densities ρ_A and ρ_B, respectively. If emission of ions or electrons from an area A is observed, the number of atoms of A and B present in the area under observation per unit depth is N_A and N_B, respectively. The probability of our probing beam interacting with particles of type B is then given by

$$P_B = \frac{N_B}{N_A + N_B} = x_B . \qquad (7)$$

The rate of interactions of the probing beam per second in the area under study is given by the incident flux Γ multiplied by the cross section σ, a measure of the probability of the interaction leading to detection. If events from the interaction are collected over a time interval Δt, the number of interactions with component B is

$$I_B = \sigma x_B \Gamma \Delta t . \qquad (8)$$

If the count noise, the flux, and the cross section are fixed, the theoretical lower limit for the detection is established:

$$x_B \geq \frac{I_B}{\sigma \Gamma \Delta t}. \qquad (9)$$

From this expression, one can see that the lower limit of the fraction of the component to be detected can be decreased by increasing the probing flux, increasing the collection time, increasing the cross section for the interaction, and reducing the noise in the counts. Most of the time, the cross section of the interaction and the background noise cannot be modified, however, so the only parameter left to modify is the probing dose. The range of probing dose depends on the excitation source used, the acquisition time, and the criteria for damage to the specimen if the probing beam is capable of damaging the sample. In addition, effects of detection efficiency and line width should be considered. A fine example of the sensitivity in LEISS measurements is shown in **Fig. 12** for gold. Note that even relatively small amounts of impurities are still detected by the HESA.

F. Quartz Crystal Microbalance – Dual Crystal Unit

The quartz crystal microbalance technique is a mature and well-developed diagnostic metrology tool measuring mass loss from materials irradiated by energetic particles. Measurement of the partial sputter yield requires elemental analysis on the QCO collecting the multispecies sputtered plume material. Typically, this method requires extraction of the QCO from the vacuum chamber for ex situ analysis or postirradiation analysis in the IMPACT experiment. This process not only is time consuming but also exposes the QCO sample to atmosphere. In order to address this issue, the QCM-DCU is installed on a predesigned port of the IMPACT vacuum chamber. In QCM-DCU, one crystal oscillator measures deposition from an eroding surface, while the second measures the background ambient simultaneously. This approach also contends with the

variability of the oscillators with background system pressure and long-temporal, temperature-dependent effects. Background ambient changes can be picked up by the ultra-sensitive oscillator. Thus, when measuring ML deposition over a relatively small dose, the use of a deposition and reference oscillator system can improve measurement accuracy.

A special port was designed to allow in situ surface analysis of the QCO without evacuation. The port lies at an angle of 145° with respect to the chamber longitudinal axis; and when spun 180°, the QCO is rotated to the main sample (after retracting the sample) location exposing the QCO to all surface analysis techniques, as shown in **Fig. 13**. **Figure 14** shows the specific geometry of the QCM-DCU system with respect to the sample location. When the QCM-DCU is rotated 180°, the geometrical center of the chamber is on the face of the QCO. The face of the QCO is tangent to a cylinder with 9.0 ± 0.1 mm radius, with its axis inclined 55° with respect to the sample plane when the sample is not tilted. The axis of rotation of the sample is perpendicular to the axis of the QCO position cylinder, so the relative angle between the face of the QCO and the surface can be changed by rotating the sample.

The rotating QCM-DCU setup in IMPACT offers additional advantages. One advantage is the ability to measure the collected fraction at multiple points in the space surrounding the sample. This measurement can ultimately lead to an estimate of the sputtered angular distribution of eroded species. **Figure 14** shows a schematic of the rotating QCM-DCU geometry with the QCO in three positions, illustrating the orientation of the QCM-DCU with respect to a sample with no tilt and the sign conventions for the positioning of the QCM-DCU. The position of the center of the QCM-DCU system is specified by a vector in cylindrical coordinates (R, z, θ), where R is the fixed radial position of the QCM-DCU on the cylinder, 9 mm. The value of z is set to 0 at the point where a normal from the center of the QCO intersects the center of the

sample, and the positive z direction indicates insertion into the chamber past this point. The value of $\theta = 0$ is set when the center of the sample and the center of the QCO lie on the same vertical plane. The problem is reduced to the following: Given the pair (z,θ), express the integral: $\int_{\Omega_{QCM}} f(\Omega)d\Omega$ in terms of those two parameters. Here, $f(\Omega)$ is an angular function representing the sputtering flux, and Ω_{QCM} is the solid angle subtended by the QCM-DCU collection oscillator crystal. The procedure to perform the integral over the area of the QCM is detailed in two other publications.[15,16]

III. Analytical Diagnostic Tools

IMPACT uses several in situ metrology techniques that are able to measure the local surface atomic concentration of implanted or deposited Sn atoms during either exposure to ions or thermal atoms, respectively. The in situ techniques include LEISS, AES, XPS, and EUPS. All these techniques can interrogate the sample during exposure at various depths. A schematic of the various surface characterization techniques in IMPACT probing two separate spatial scales at the surface is given in **Fig. 15.** LEISS gives compositional information about the top monolayer in the sample, while AES and XPS probe the subsurface layers using kinetic electrons and emitted photoelectrons, respectively. The techniques are complementary and allow a more reliable identification of components as well as their relative abundance and chemical state. More details of the various surface analysis tools used in the IMPACT are given in the following subsections.

A. Low-Energy Ion Scattering and Direct-Recoil Spectroscopy

Low-energy ion scattering spectroscopy is one of the few real-space techniques able to probe the first and second monolayer of a surface.[3,13] Such probing is possible because of the higher ion-atom cross sections and high neutralization rates for probing noble-gas scattering ions. With the use of an electrostatic energy analyzer, the energy of the scattered ions can be determined; and with the use of binary collision theory, the mass of the atom from which the ions scattered can be determined. With the laboratory frame of reference and neglecting energy dissipation during the collision, the conservation equations yield an expression that relates the incident particle energy, E_o, and incident and target masses, M_1 and M_2, with the scattered particle energy, E_1, and the angle, θ, between the initial and final directions of the incident particle:

$$E_1 = E_0\left(\frac{M_1}{M_1+M_2}\right)^2\left(\cos\theta \pm \sqrt{\left(\frac{M_2}{M_1}\right)^2 - \sin^2\theta}\right)^2 = KE_0 . \qquad (10)$$

By defining the target to projectile mass ratio $\gamma = M_2/M_1$, equation (10) can be rewritten as[3]

$$K = \left(\frac{1}{1+\gamma}\right)^2\left(\cos\theta \pm \sqrt{\gamma^2 - \sin^2\theta}\right)^2 . \qquad (11)$$

K is called the kinematic factor, and it gives the fraction of the incident ion energy retained by the scattered ion. Equation 11 solves for M_2 if all the other parameters (E_o, M_1, and θ) are known.

Figure 16 shows a plot of the kinematic factor for various scattering angles and mass ratios greater than 1. **Figure 17** shows the relation in Eq. 10 plotted as circles in a polar coordinate system. Each circle's size represents a particular mass ratio. For example, the dotted semicircle in **Fig. 17** represents a mass ratio of 1.0. The thick straight lines represent the laboratory scattering angles in IMPACT. As the circles get closer, the mass resolution becomes

worse.

Figure 16 clearly shows that, in order to obtain the best mass resolution, large scattering angles and low mass ratios are desirable. The mass ratio can be modified by choosing the mass of the probing beam; however, inert ions of high Z are more prone to neutralization because of their low ionization potentials. The use of neon as the probing beam ensures that the value of γ is kept below 10 for all target elements up to mass 200, which translates into better mass separation. The downside of using a heavier element, such as Ne, is that it will not scatter off lighter elements (i.e., H,C,N,O), so these lighter elements are visible only in the form of direct recoils that can get detected (direct recoil spectroscopy) in forward geometry. In addition, its relatively higher sputter yield makes it difficult to work with.

Target atoms knocked out of the surface and having a recoiling angle ϕ also carry a particular energy depending on their mass and the scattering angle of the incident particle. Just as the kinematic factor was calculated, the energy transfer factor *T* can be calculated for these recoil atoms. The following expression can be derived for the energy transfer factor *T*:

$$T = \frac{E_2}{E_0} = \frac{4\gamma}{(1+\gamma)^2}\cos^2\phi\,. \qquad (12)$$

The energy transfer factor for different mass ratios and recoiling angles is plotted in **Figs. 18** and **19,** respectively. Direct recoils detect low-mass atoms with heavy projectiles. We note, however, that no direct recoils can exist for angles greater that 90°, in order to satisfy the conservation of momentum.

We use primarily two types of ion beams to conduct ISS and DRS analysis in IMPACT: He^+ ion beams with energies between 1 keV and 5 keV, and Ne^+ ion beams at 2 keV, both produced with a NTI 1401 ion source. The purpose of using two different gases for sources of

ions is that the heavier the ion beam, 20 amu for Ne^+ and 4 amu for He^+, the better the mass resolution attained for larger mass atoms. For studies on heavy-ion implants in high-Z materials, this is an important factor because masses between Sn and Ru or Mo are close and optimization of mass resolution is important.

In addition to the kinematic aspects of the collisions, the fact that scattering events are stochastic implies that there is a probability associated with a scattering event at a certain angle. The probability will depend on the energy, the masses of the particles involved, and the type of interaction potential between them. The definition of the scattering cross section accounts for this probability. The scattering cross section decreases with increasing target mass and increasing projectile energy. To find the cross section values, Dr. Robert Bastasz of Sandia National Laboratory at Livermore wrote a computer code that uses angular differential scattering cross-section equations.[17] The scattering formula used in the code is Gauss-Mehler quadrature, and both screening and potential functions are ZBL. Knowledge of the energy corresponding to each target mass and the cross section σ for the corresponding projectile-target pair yields calculation of the sample surface composition. Therefore, during an energy scan with the detector, N number of peaks each with area A_i are observed. The atomic fraction of each component y_i can be calculated by

$$y_i = \frac{A_i \sigma_i^{-1}}{\sum_{k=1}^{N} A_k \sigma_k^{-1}} \,. \qquad (13)$$

In order to minimize sputtering, ion currents on the order of hundreds of nanoamperes or lower are used.

As part of the calibration effort of the ISS and DRS techniques implemented in IMPACT, measurements of scattered 1 keV He^+ were performed on pure materials in order to compare the values obtained in practice for the scattered particle energy with values from elastic collision theory. The scattering angle was set to 90° by installing the ion beam source perpendicular to the detector's line of sight. Results of LEISS spectra are shown in **Fig. 20**. The straight solid lines show the expected theoretical locations on the energy spectrum of corresponding masses measured. The data shows that the measured energy is always lower than the energy predicted by elastic collision theory. The shifts are always lower than 10% in energy, but even small shifts can mean large uncertainty (~20%) in the mass as a result of poor mass resolution at the higher energies. The shifts are due to inelastic energy losses during the scattering event and variation in the angle between the beam and the detector.

Inelastic energy losses are not uncommon and are handled by design of specific experiments able to measure such losses.[18] Nevertheless, semiquantitative analysis is possible with LEISS because the losses are known when comparing to peaks such as oxygen or other elements known to exist in the sample analyzed. In addition, IMPACT utilizes more than one surface analysis technique to ensure that element identification is properly obtained and verified. Further work on assessing inelastic losses in samples studied in IMPACT are ongoing and the subject of a future paper.

B. Electron Spectroscopies

IMPACT applies three types of electron spectroscopies that probe varied spatial scales at the surface of ultra-thin film systems. The first is high-resolution x-ray photoelectron spectroscopy using the dual anode x-ray source described earlier, the second is typical Auger

analysis, and the third is EUV photoelectron spectroscopy. This section focuses on the first two techniques used in conjunction with other surface characterization tools in IMPACT. Both XPS and AES are useful for determining atomic surface composition using different procedures of quantitative analysis, and they are complementary.[19,20]

XPS involves the energy analysis of the photoelectrons created by x-ray radiation. XPS line shape analysis provides qualitative information and identification of changes in the chemical state of atoms and complex molecules, and hence it is a versatile tool for in situ surface analysis. The ability to perform XPS is valuable when studies regarding the chemical state of elements are important, since photoelectron lines shift when elements are in a chemically bound state compared to the pure element. These chemical shifts range from fractions of an electron volt to a few electron volts. The resolution of chemical shifts strongly depends on the energy spread of the measured peak and the magnitude of the shift. An example of XPS in situ diagnostics in IMPACT is depicted in **Fig. 21,** which gives the XPS spectra obtained from a Ru sample deposited with thermal Sn. The two spectra given in the figure were recorded under identical conditions except that the second spectrum taken after exposing the sample to air. The inset in the figure shows that the Sn 3d peaks are shifted toward the higher binding energy levels as a result of oxidation. This clearly points out the importance of in situ surface analysis.

In surface analysis, it is advantageous to have high spatial resolution of the system. We examined the spatial resolution obtainable with IMPACT XPS system. Two basic approaches for obtaining highest spatial resolution for XPS are manipulating the source and/or manipulating the detector parameters. The x-ray source in IMPACT is non-monochromatic and hence not collimated. Thus, the x-rays flood the entire sample area (~ 1 × 1 cm^2), and photoelectrons are emitted from all places in the sample. The optical elements on the energy analyzer can be used

for narrowing the field of view of the detector. The base resolution of a spectrometer is given by the following equation:[21]

$$I \propto \frac{\pi}{4}\left(\frac{r}{M}\right)^2 \alpha\beta\,, \qquad (14)$$

where I, r, M are the transmitted intensity, the diameter of the input aperture, and the magnification of the transfer lens, respectively, and α and β correspond to acceptance angles in the dispersion and nondispersion directions. The above relation shows that, in the absence of spherical aberration, the spatial resolution is r/M. The transfer lens system in the detector can provide a maximum magnification of 10, and the entrance slit diameter widths can be varied from 1 mm upward. Hence the best spatial resolution obtainable with our XPS is ~ 100 μm after discarding all aberrations caused by the lens system. But there exists a tradeoff between the electron flux and slit value. With the narrowest slit configuration (1 mm), the electron flux reaching the detector is very low. Therefore, we chose a configuration of M = 10 and r = 3 mm for our measurements, which leads to a theoretical spatial resolution of 300 μm after discarding aberrational effects.

To test this capability, we selected a reference sample containing a strip of Teflon with 1.3 mm width. The sample holder in the IMPACT system can provide a translation movement with resolution better than 10 μm. F 1s XPS line scans were taken across the target with 150 μm spatial intervals and with a 50 eV pass energy. **Figure 22** shows the XPS line scan across the sample surface, indicating a spatial resolution better than 500 μm.

IMPACT is also equipped with AES for surface analysis. The excitation source for AES is an electron gun. AES is the energy analysis of the Auger electron generated by the electron beam. Similar to XPS, AES is typically used for elemental identification, line scans, and other

quantitative information. Whereas XPS can analyze nonconducting materials such as plastics and ceramics with minimum charging effects and can investigate differences in the chemical state and bonding in the elements. AES is superior in terms of higher spatial resolution because of the smaller electron-beam size at the target.

C. In Situ Erosion Rate Measurement

IMPACT has a quartz crystal microbalance – dual crystal unit diagnostic system for in situ real-time total erosion measurements to allow for a direct conversion from time to spatial scales during depth profiling with our in situ surface analysis metrology. The QCM-DCU diagnostic system measures the total sputtering yield induced by energetic charged particles. Quartz crystal microbalances have been used in various configurations to measure small changes in mass during erosion induced by particle bombardment.[22] IMPACT utilizes the QCM diagnostic in collection geometry of sputtered particles as opposed to direct sputter rate measurement by bombarding a predeposited film on the quartz crystal oscillator surface. For multicomponent samples, only the combined mass erosion yield is measured by the QCM-DCU.

Details of the QCM-DCU technique are given in Section II-F. The collected fraction, assuming $f(\Omega)$ to be a pure cosine distribution, is plotted as a function of the parameters z and θ in **Fig. 23**. Two cases are plotted: **Fig. 23(a)** shows the collected fraction for a 0° tilt (i.e., normal) sample, while **Fig. 23(b)** shows the collected fraction for the case of a sample tilted 55°, such that the face of the QCM and the sample surface are parallel. The angular distribution of sputtered particles can be inferred from a set of experimental measurements at different values of z and θ; this technique will be discussed in detail in a future publication.[23]

Another advantage of the QCM-DCU system is the ability to measure the erosion rate from mixed materials and redeposited materials. This measurement can be done in several ways.

One is to have a polycrystalline thin-film deposited on the QCO prior to UHV chamber insertion or deposition in situ by exposing the QCO to a sputter target located at the IMPACT sample holder location. Once the film is deposited, a second sputter target can be inserted and bombarded by any of the ion sources available in IMPACT, thus yielding a "mixed" material surface. This type of surface is similar to the types found on PFC surfaces in fusion tokamak devices.[24] Once the mixed material surface is prepared, ion-induced sputtering can be measured from this mixed-material surface and tracked by several techniques in situ and in real time: (1) direct sputter yield measurement from mass loss off the QCO, (2) mass spectrometry during irradiation, (3) surface analysis using LEISS, XPS, EUPS, or AES, and (4) soft x-ray reflectometry for structure determination. Another method for studying redeposited surfaces is to attach a witness plate (typically a specific material desired for study) on the QCM-DCU holder in place of the QCO. This technique allows the use only of surface analysis measurements and is considered useful for only limited cases.

D. In Situ EUV Reflectometry

One of the unique capabilities of the IMPACT facility is the ability to monitor the EUV reflectivity of thin metal films as they are modified by an ion beam, a thermal flux, or a combination of both. This capability of IMPACT has already provided important insights relevant to the operation of collector mirrors used in Sn plasma EUV light sources for nanolithography.[7,11]

The EUV source installed in the IMPACT facility emits radiation at 13.5 nm ± 1 nm. The cone of light leaving the source needs to be collected and transported to the sample. For that purpose, an elliptical mirror is used. Since we are dealing with EUV radiation that is easily

absorbed by most materials, only reflective components can be used. An elliptical mirror with radius of curvature 0.5 m is chosen to focus the EUV light to a spot of a few millimeters on the IMPACT target surface location, and the half-angle used is 15° with respect to the mirror surface. The collector mirror was manufactured by carving the rough elliptical shape on an aluminum block. The block was electroplated with nickel and then diamond-turned to give it the final elliptical shape with an accuracy of 0.002 mm. A reflective 50 nm Ru coating was applied to the Ni mirror at the Optics Fabrication and Metrology laboratory at Argonne's Advanced Photon Source. The mirror is mounted on a linear manipulator to allow for small focusing corrections.

The geometry of the reflectometer is sketched in **Fig. 24.** Three ports on the IMPACT chamber are situated in such a way that when the sample is tilted at 45°, the three ports lie in the same plane. This tilt allows the sample to be probed with any of the surface analysis techniques while the EUV reflectivity is being measured. The half-angle for the reflectivity measurement is 15° with respect to the plane of the sample. When the sample is retracted, the light can be collected by a separate detector, which can be used to monitor the photon flux coming from the source.

The detectors used in the reflectometer are photodiodes with a 1 x 1 cm active area and a deposited Si/Mo filter with a spectral band of 10 nm to 16 nm photons. This filter greatly reduces the signal due to stray light, but a dark chamber is still required to perform the measurement. During measurements, typical photocurrents are in the order of 100 pA. By assuming a quantum efficiency of 1 on the photodiode, this corresponds to a photon current of 6×10^8 photons/s. This is roughly 10 times lower than the output expected from the source. If the sample is bypassed, the current read in the photodiode can reach 400–600 pA, which is on the order of the level

expected from the source. Small misalignments exist on the reflectometer setup, a fact evident from **Fig. 25**, where the photocurrent intensity is plotted as a function of sample tilt. If all components of the reflectometer were aligned, the peak photocurrent should occur at a tilt of 45°. Small misalignments in the EUV spot location or angle of incidence may be responsible for this change in the nominal tilt value. Despite this small change, the relative reflectivity measurements can still be performed as long as the conditions of the reflectometer (source position, sample tilt, power output, photodiode efficiency) remain the same during the experiment.

To obtain the relative at-wavelength (13.5 nm) EUV reflectivity as the sample is modified (e.g., temperature, Sn exposure), consider a sample property that changes with time as *f(t)* when the sample undergoes a certain treatment. Before the treatment, the value of the photocurrent at the reflectivity detector is recorded as I_0. Both the quantity f and the photocurrent I are measured at a time interval Δt. Then, the reflectivity change due to the change in the property f is obtained by applying the chain rule:

$$\frac{dI}{df} = \frac{dI}{dt}\frac{dt}{df} = \frac{dI}{dt}\left(\frac{df}{dt}\right)^{-1} . \tag{15}$$

By assuming that nothing in the reflectometer changes over the course of the experiment, the relative reflectivity R at any time t is given simply by

$$R(t) = \frac{I(t)}{I_0} . \tag{16}$$

Similarly, the change in reflectivity due to changes in the property f is given by

$$\frac{dR}{df} = \frac{1}{I_0}\frac{dI}{df} . \tag{17}$$

During the experiment, the mechanical components of the reflectometer do not move, since all the components – with the exception of the sample under study – are secured to their

position. Hence, the only possible variation on the measured reflected intensity can be attributed to fluctuations in the EUV power coming from the source. This is typically not the case for the source, except near the end of life of the electron emitter on the source. The stability of the EUV power output can be checked during the experiment by monitoring the photodiode located in the line-of-sight of the focused EUV light. If variations on the source power output are observed, the reflectivity can still be calculated if the line-of-sight photocurrent I_{ref} is known as a function of time:

$$R(t) = \frac{I(t)}{I_{ref}(t)} \frac{I_{ref}(0)}{I(0)} . \qquad (18)$$

The most important assumption in deriving this equation is that any fluctuation on the output power causes a corresponding fluctuation of the reflected signal, and the ratio of these two fluctuations is constant. This can be assumed to be true if none of the reflectometer components is moved during the course of the experiment and if the sample can be brought back to the same spot after retracting it out of the way to measure the reference current. In addition, off-specular scattering has some probability of introducing error in the specular signal. This has been found to be a minor effect, however, as the specularly reflected light is collected only at the photodiode. Any loss due to off-specular scattering would be manifested in a loss in specular reflection measured by the photodiode during sample measurement.

IV. RESULTS AND DISCUSSION

A controlled experiment was used to demonstrate the capabilities of complementary surface characterization techniques used in the IMPACT facility. The surface was actively probed in situ by using XPS, low-energy ISS in backscattering mode, QCM-DCU, and EUV reflectometry. The results, shown for thin transition-metal films (Rh, Ru, and Pd), focus on the role thermal vs

energetic Sn has on the surface atomic concentration on the mirror surface and the 13.5 nm relative EUV reflectivity.

The first case consists of a Rh mirror exposed to a source of thermal Sn from the EGN4 e-beam evaporator. Data was taken during exposure of both LEISS and XPS. Simultaneously we measured the effect on 13.5 nm EUV reflectivity with the EUVR system. **Figure 26(a)** shows the surface Sn atomic fraction reaching a steady state value of 90–100% coverage at a Sn fluence of about 10^{16} cm^{-2}. **Figure 26(b)** shows the effect on the relative 13.5 nm reflectivity during deposition. A comparison is made to the theoretical Fresnel reflectivity using IMD simulations, which assume layer-by-layer growth (Frank van der Merwe type). That is, a full monolayer is grown, and 100% Sn coverage is reached after a fluence of 10^{15} Sn/cm^2. The results show clearly that the measured 13.5 nm reflectivity is distinctly different from the theoretical specular reflectivity from an ideal full Sn layer, suggesting that the morphology and structure of the deposited Sn film are inherently different from a van der Merwe-type grown layer. Further details of the implications of these results are to be published elsewhere. [23]

The next case studied concerns the exposure of Ru mirror surfaces to energetic Sn particles. For these experiments 1.3 keV Sn^+ was exposed to an identical Rh mirror at 0° with respect to the mirror surface normal. Both the Sn surface atomic fraction measured with LEISS and the relative 13.5 nm EUV reflectivity loss measured with EUVR are shown in **Fig. 27** and compared to the thermal-deposited Sn exposures. Energetic Sn at 1.3 keV is found to implant at 2-3 ML into the mirror surface. Because of a balance between implantation and ion-induced sputtering, the Sn surface atomic fraction reaches a steady-state surface concentration that is lower in magnitude than that from Sn vapor deposition. The measured fraction is about 60–70% and is reached after a Sn ion fluence of about 0.2–0.3 x 10^{16} cm^{-2}. Although the EUV 13.5 nm

relative reflectivity seems to decrease at the same rate for both thermal and energetic Sn exposure, at larger fluences reflectivity from the Sn-deposited surface is found to decrease to levels near 40% compared to steady-state levels of > 90% with samples exposed to energetic Sn. This difference is significant and elucidates the distinct mechanisms between thermal and energetic Sn on the ultra-shallow region at the surface of these candidate mirror materials (Ru, Rh, or Pd).

Another attractive feature of the IMPACT experimental facility is its ability to measure in situ the energetic particle-induced erosion rate (sputtering). Recall that this is achieved by a QCM-DCU installed on a rotating-translational manipulator system. In this section we consider the *total* absolute sputtering yield measurement of particles eroded by energetic Sn. A more comprehensive analysis of preferential sputtering is beyond the scope of this paper and is highlighted in a separate publication.[11] For the case shown above we considered the sputtering induced by energetic Sn on a Ru mirror sample, which demonstrates identical response to Rh EUV light collector mirrors. During exposure to 1.3 keV Sn^+ the sputtered material was collected by the QCM-DCU and the sputter rate recorded as a function of time (fluence). **Figure 28** shows the raw data from the frequency variation as a function of time (fluence). Precleaning was conducted and the mirror then exposed to Sn ions at 1.3 keV rastered at normal incidence in a 0.25 cm^2 area. Using 6.2 g/cm^3 and 4.2 g/cm^3 for the densities of the QCO and Sn eroded film, respectively, we calculated the erosion rate to be about 0.66 nm/sec. We note that the irradiation with Sn ions is noncontinuous, so LEISS and XPS data can be taken between exposures. Therefore the total irradiation time is only about 30 minutes.

In summary, the IMPACT experimental facility has been designed for versatility in measuring the response of heterogeneous surfaces to a combination of particle sources. By

combining Sn thermal atoms and energetic Sn, we have demonstrated the capability of IMPACT's in situ surface diagnosis, including XPS, LEISS, QCM-DCU, and EUVR. The combination of multiple diagnostic systems has identified key mechanisms in the degradation of optical mirror thin-film surfaces during exposure to Sn debris.

ACKNOWLEDGMENTS

We thank V. Titov and W. Klimowych for work in the PRIME facility. We thank our SULI students (Science Undergraduate Laboratory Internships) partly sponsored by the Department of Energy: S. Taj, D. Rokusek, C. Chrobak, E. Hinson, W. Lytle, S. Benario, H. Nomanbhai, M. Hull, and D. Detert. We thank Ph.D. student M. van der Velden, of TU Eindhoven for work on threshold sputtering. We thank our collaborators on EUV lithography work: Philips Research Laboratories in Aachen; Fraunhöfer Insitut in Aachen; ASML; Xtreme Technologies; R. Bastasz at SNLL; NIST-SURF facility; O. Auciello, A. Macrander, and the OFM-APS team; R. Majeski and R. Kaita at PPPL; and R. Doerner and M. Tillack at UCSD. We thank A. Egbert of Phoenix EUV for providing EUV source performance data. This work was supported in part by the U.S. Dept. of Energy under Contract DE-AC02-06CH11357.

REFERENCES

[1] O. Auciello, A. R. Krauss, J. Im, and J. A. Schultz, Ann. Rev. Mat. Sci. **28,** 375 (1998).

[2] W. Jacob, C. Hopf, A. von Keudell, M. Meier, and T. Schwarz-Selinger, Rev. Sci. Instrum. **74,** 5123 (2003).

[3] J. Wayne Rabalais, *Principles and Applications of Ion Scattering Spectrometry: Surface and Chemical and Structural Analysis* (John Wiley & Son, Inc., New Jersy, 2003).

[4] A. Hassanein, V. Sizyuk, V. Tolkach, V. Morozov, and B. Rice, J. Microlith. Microfab. Microsys. **3,** 130 (2004).

[5] V. Sizyuk, A. Hassanein, and T. Sizyuk, J. Appl. Phys. **100,** Art. no.103106 (2006).

[6] V. Sizyuk, A. Hassanein, and T. Sizyuk, Las. Part. Beams **25,** 143 (2007).

[7] J. P. Allain, A. Hassanein, M. M. C. Allain, B. J. Heuser, M. Nieto, C. Chrobak, D. Rokusek, and B. Rice, Nucl. Instrum. Meth. B-Beam Inter.Mat.Atm. **242,** 520 (2006).

[8] J. P. Allain, A. Hassanein, M. Nieto, V. Titov, P. Plotkin, E. Hinson, B. J. Rice, R. Bristol, D. Rokusek, W. Lytle, B. J. Heuser, M. M. C. Allain, J. Hyunsu, and C. Chrobak, Proc. SPIE **5751,** 1110 (2005).

[9] S. S. Harilal, B. O'Shay, Y. Tao, and M. S. Tillack, Appl. Phys. B - Las. & Opt. **86,** 547 (2007).

[10] A. Hassanein, T. Burtseva, J. N. Brooks, I. K. Konkashbaev, and B. J. Rice, Proc. SPIE **5037,** 358 (2003).

[11] M. Nieto, J. P. Allain, V. Titov, M. R. Hendricks, A. Hassanein, D. Rokusek, C. Chrobak, C. Tarrio, Y. Barad, S. Grantham, T. B. Lucatorto, and B. Rice, J. Appl. Phys. **100,** Art. no. 053510 (2006).

[12] J. P. Allain, J. N. Brooks, D. A. Alman, and L. E. Gonzalez, J. Nucl. Mat. **337-39,** 94 (2005).

[13] H. Niehus, W. Heiland, and E. Taglauer, Surface Science Reports **17,** 213 (1993).

[14] A. Egbert, B. Mader, B. Tkachenko, A. Ostendorf, C. Fallnich, B. N. Chichkov, T. Missalla, M. C. Schurmann, K. Gabel, G. Schriever, and U. Stamm, J. Microlith. Microfab. Microsys. **2,** 136 (2003).

[15] J. P. Allain, D. N. Ruzic, and M. R. Hendricks, J. Nucl. Mat. **290,** 180 (2001).

[16] J. P. Allain, D. G. Whyte, and J. N. Brooks, Nucl. Fusion **44,** 655 (2004).

[17] R. Bastasz and W. Eckstein, *Common Concepts: Particle Scattering - Methods of Materials Research* (Wiley, New York, 2000).

[18] M. D. Coventry, J. P. Allain, and D. N. Ruzic, J. Nucl. Mat. **335,** 115 (2004).

[19] P. J. Cumpson and M. P. Seah, Surface and Interface Analysis **25,** 430 (1997).

[20] W. S. M. Werner, Appl. Surf. Sci. **235,** 2 (2004).

[21] M. P. Seah and G. C. Smith, Surf. Interf. Anal. **11,** 69 (1988).

[22] G. Hayderer, M. Schmid, P. Varga, H. P. Winter, and F. Aumayr, Rev. Sci. Instrum. **70,** 3696 (1999).

[23] J. P. Allain et. al**,** to be published (2007).

[24] A. Hassanein, J. P. Allain, Z. Insepov, and I. Konkashbaev, Fusion Science and Technology **47,** 686 (2005).

FIGURE CAPTIONS

FIG. 1. Schematic of the IMPACT experimental facility with selected excitation sources and in situ diagnostic systems.

FIG. 2. Plot of ion-beam current vs energy for various ion sources.

FIG. 3. Energy spread of a 50, 100, and 150 eV Ar^+ beam measured with a retarding field analyzer.

FIG. 4. Spatial profile of singly charged ion beams at different impact energies.

FIG. 5. Helium singly charged beam profile using the 5-pinhole Faraday cup diagnostic in IMPACT.

FIG. 6. Retarding field analyzer for the measurement of energy spread and beam profile of ions generated by IMPACT ion sources.

FIG. 7. Energy spread of 150 eV argon and xenon singly charged ion beams.

FIG. 8. Layout and scales for the EUV spot-size measurement experiment.

FIG. 9. Photocurrent measured by the detector in the reflecting location. The results of the measurements are shown for the sample orientation shown in Fig. 8 (filled symbols) and after rotating the sample 90° counterclockwise (empty symbols).

FIG. 10. QCM response to the Sn deposition for different flux levels from the evaporator.

FIG. 11. Comparison of the deposition rates of the Sn evaporator operating with (open triangles, right ordinate) and without the nozzle (closed squares, left ordinate). The deposition is reduced by a factor of 7.75 for operation with the nozzle.

FIG. 12. ISS scan taken with 1 keV He ions of a bulk Au sample using the normal scattering position (90°).

FIG. 13. Rotating QCM-DCU system in IMPACT.

FIG. 14. Geometry of the rotating QCM system, showing three different positions of the QCM that illustrate the sign convention for linear and angular displacement.

FIG. 15. Complementary surface characterization techniques in IMPACT probing two separate spatial scales at the surface.

FIG. 16. Kinematic factor as a function of scattering angle and target-to-projectile mass ratio. Mass resolution increases by increasing the scattering angle and lowering the mass ratio.

FIG. 17. Scattering kinematic circle showing the mass ratio and its dependence on the scattered angle in the laboratory frame.

FIG. 18. Energy transfer factor as a function of mass ratio and recoiling angle.

FIG. 19. Kinematic circle diagram for recoils with mass ratios and scattering angles relevant to recoil detection in the laboratory frame.

FIG. 20. ISS scans of different elements obtained by measuring the energy of 1 keV He ions scattered at 90° from the incident direction.

FIG. 21. XPS spectra obtained from Ru sample deposited with thermal Sn. Spectrum (1) recorded in situ with a Sn flux of 5×10^{16} cm^{-2}. Spectrum 2 is taken after exposing the sample to air, which led to oxidation. Inset shows the shifts in Sn 3d photoelectron peaks due to oxidation.

FIG. 22. XPS line scan across 1.3 mm wide Teflon sample. F 1s photoelectron peak at 689 eV is used.

FIG. 23. Fraction of the sputtering flux with cosine distribution collected by the QCM crystal as a function of the cylindrical coordinates (z, θ). Two sample tilts are shown: a) 0° and b) 55°.

FIG. 24. Schematic of the reflectometer setup in IMPACT. Dashed lines indicate the path of the light when the sample is retracted. Distances are shown in cm.

FIG. 25. Variation of photocurrent with the tilt of the sample. The flat top between 46.5° and 47.5° indicates that the spot on the photodiode is smaller than the active area of the detector.

FIG. 26. Estimated surface Sn atomic fraction for various thermal Sn fluences (a). It shows Sn fraction reaching a steady state value of 90–100% coverage at a Sn fluence of about 10^{16} cm^{-2}. The effect on the relative 13.5 nm reflectivity during deposition is given in (b). The solid curve in (b) corresponds to IMD theoretical Fresnel reflectivity.

FIG. 27: Sn surface atomic fraction measured with LEISS (a) and the relative 13.5 nm EUV reflectivity loss measured with the EUVR (b) for energetic and thermal Sn deposition.

FIG. 28. Raw data of QUM-DCU showing the frequency variation as a function of time collected during Rh sample exposure to 1.3 keV Sn ions.

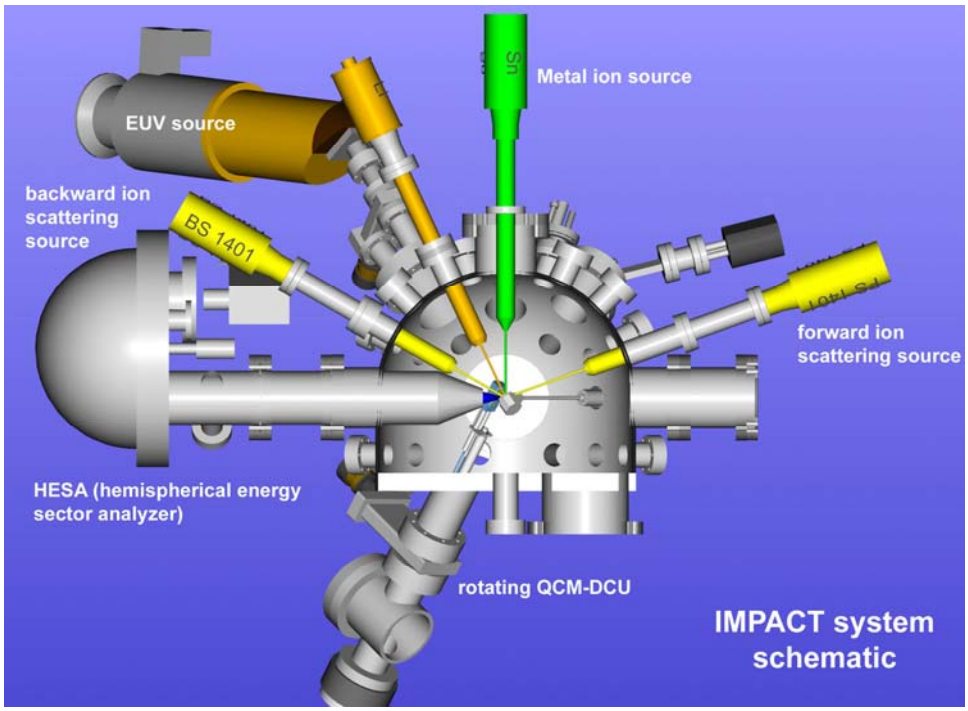

FIG. 1. Schematic of the IMPACT experimental facility with selected excitation sources and in situ diagnostic systems.

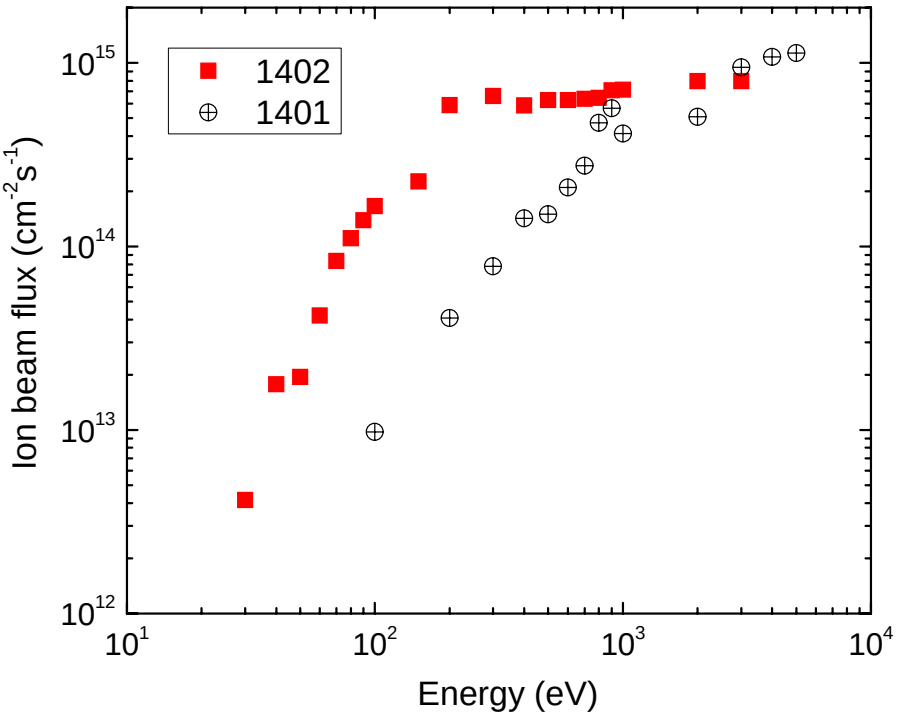

FIG. 2. Plot of ion-beam current vs energy for various ion sources.

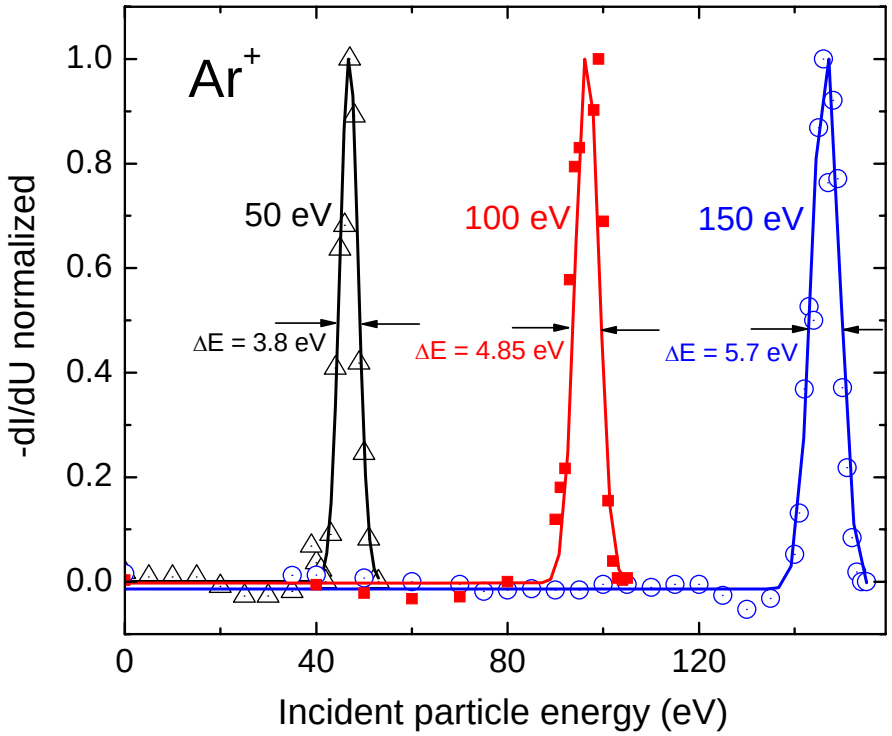

FIG. 3. Energy spread of a 50, 100, and 150 eV Ar^+ beam measured with a retarding field analyzer.

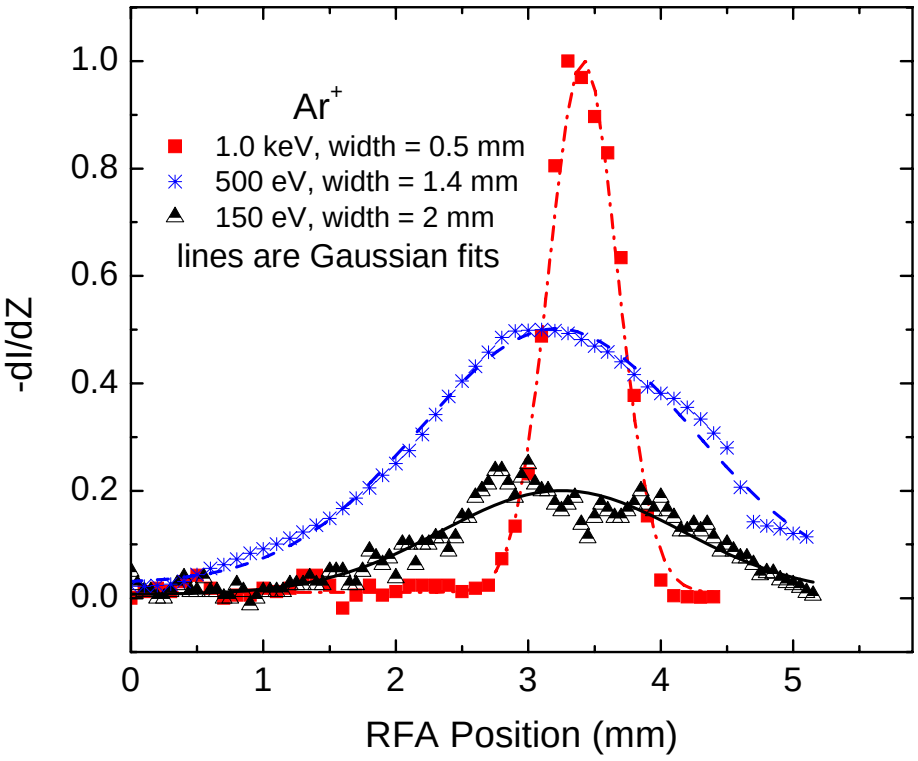

FIG. 4. Spatial profile of singly charged ion beams at different impact energies.

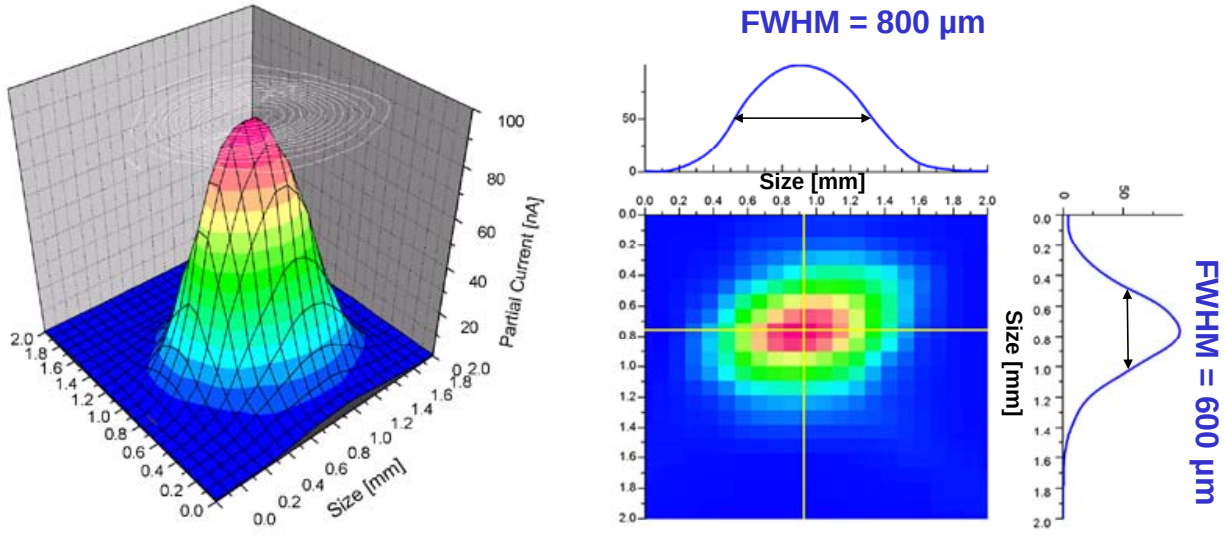

FIG. 5. Helium singly charged beam profile using the 5-pinhole Faraday cup diagnostic in IMPACT.

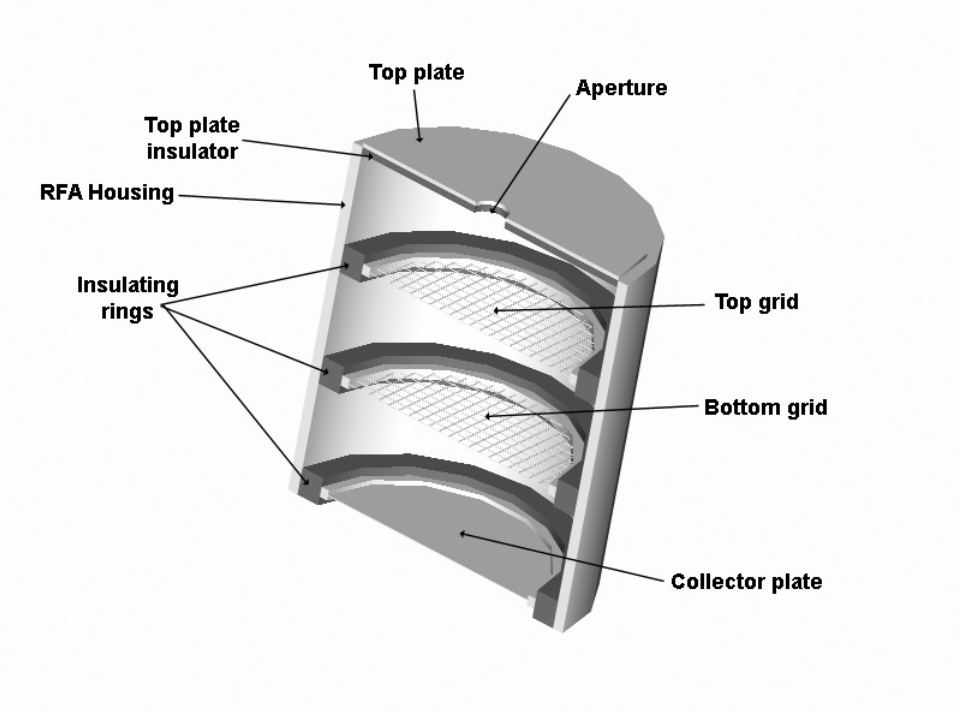

FIG. 6. Retarding field analyzer for the measurement of energy spread and beam profile of ions generated by IMPACT ion sources.

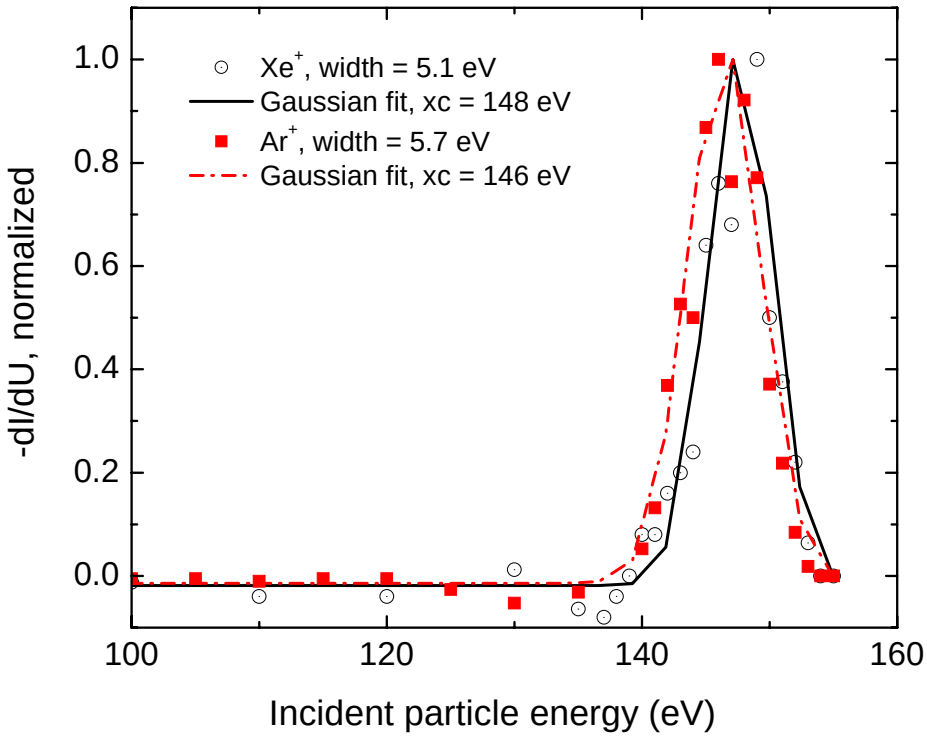

FIG. 7. Energy spread of 150 eV argon and xenon singly charged ion beams.

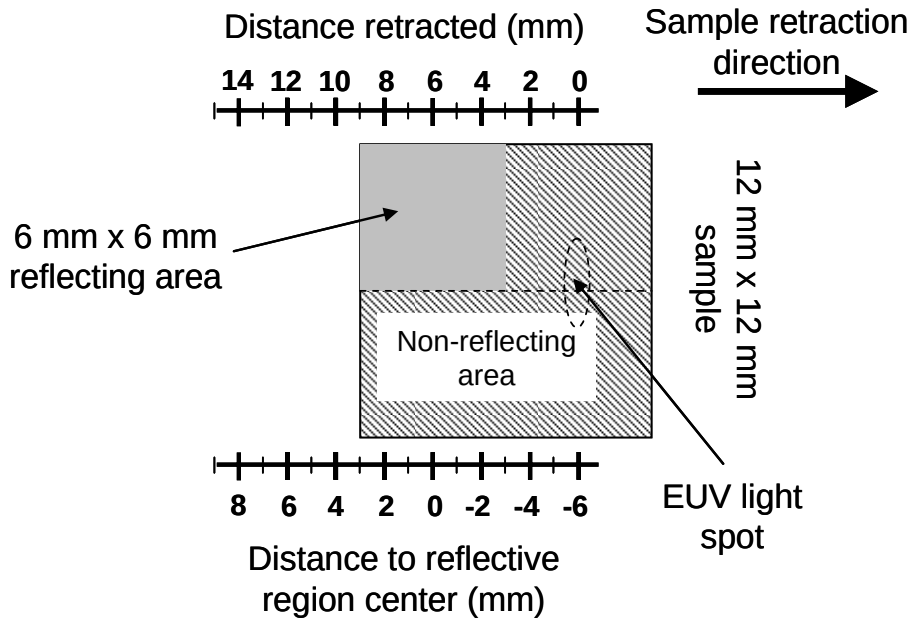

FIG. 8. Layout and scales for the EUV spot-size measurement experiment.

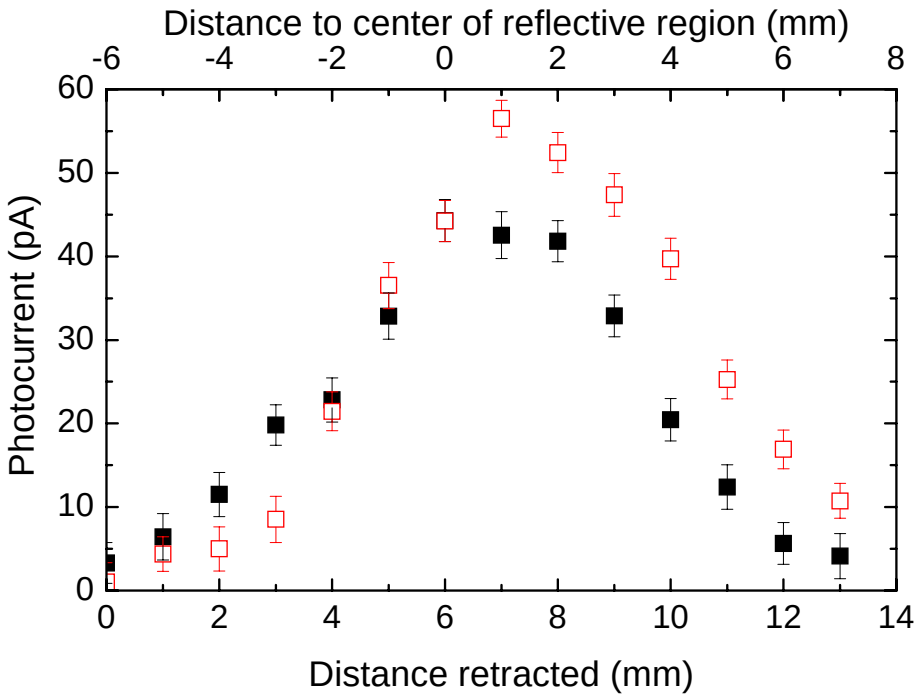

FIG. 9. Photocurrent measured by the detector in the reflecting location. The results of the measurements are shown for the sample orientation shown in Fig. 8 (filled symbols) and after rotating the sample 90° counterclockwise (empty symbols).

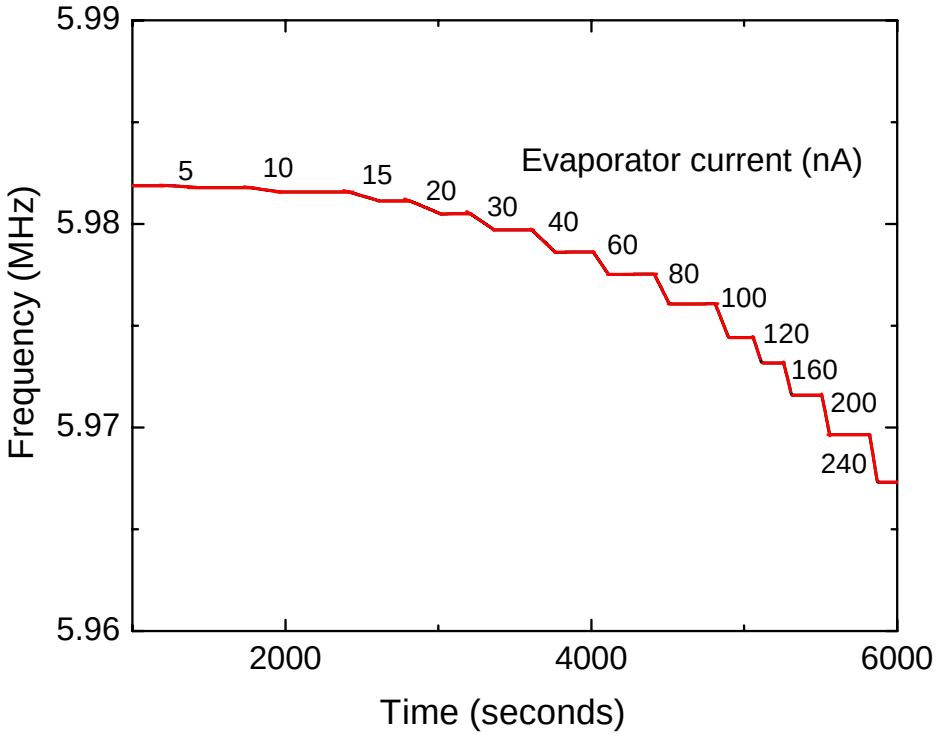

FIG. 10. QCM response to the Sn deposition for different flux levels from the evaporator.

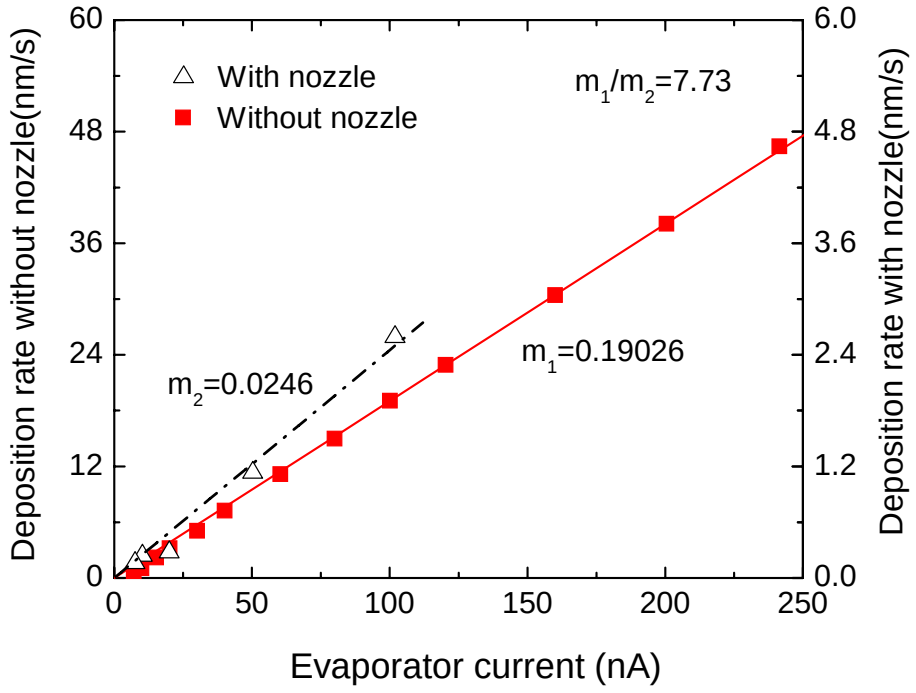

FIG. 11. Comparison of the deposition rates of the Sn evaporator operating with (open triangles, right ordinate) and without the nozzle (closed squares, left ordinate). The deposition is reduced by a factor of 7.75 for operation with the nozzle.

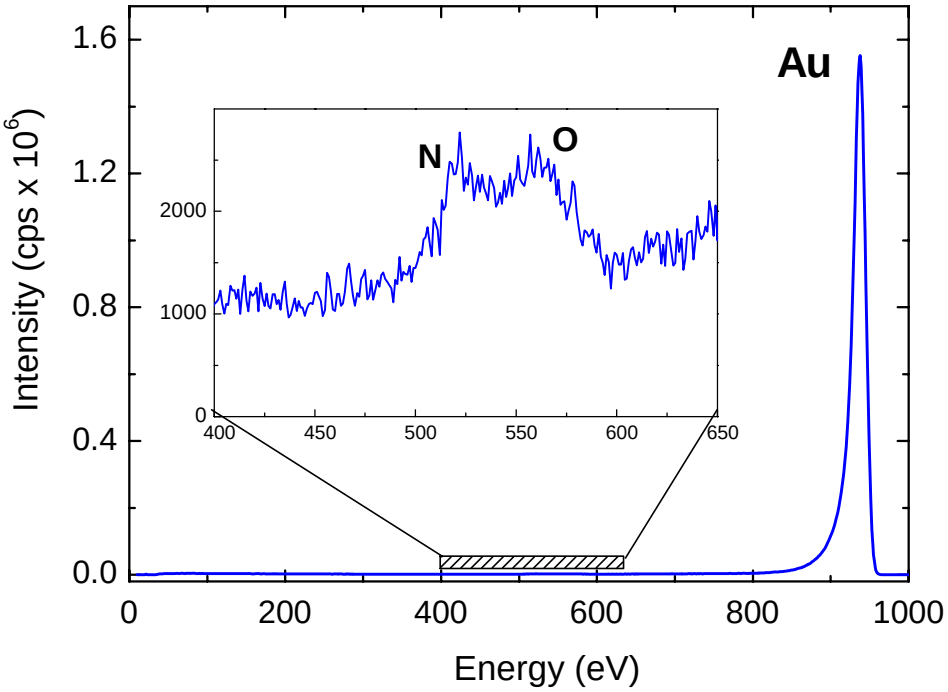

FIG. 12. ISS scan taken with 1 keV He ions of a bulk Au sample using the normal scattering position (90°).

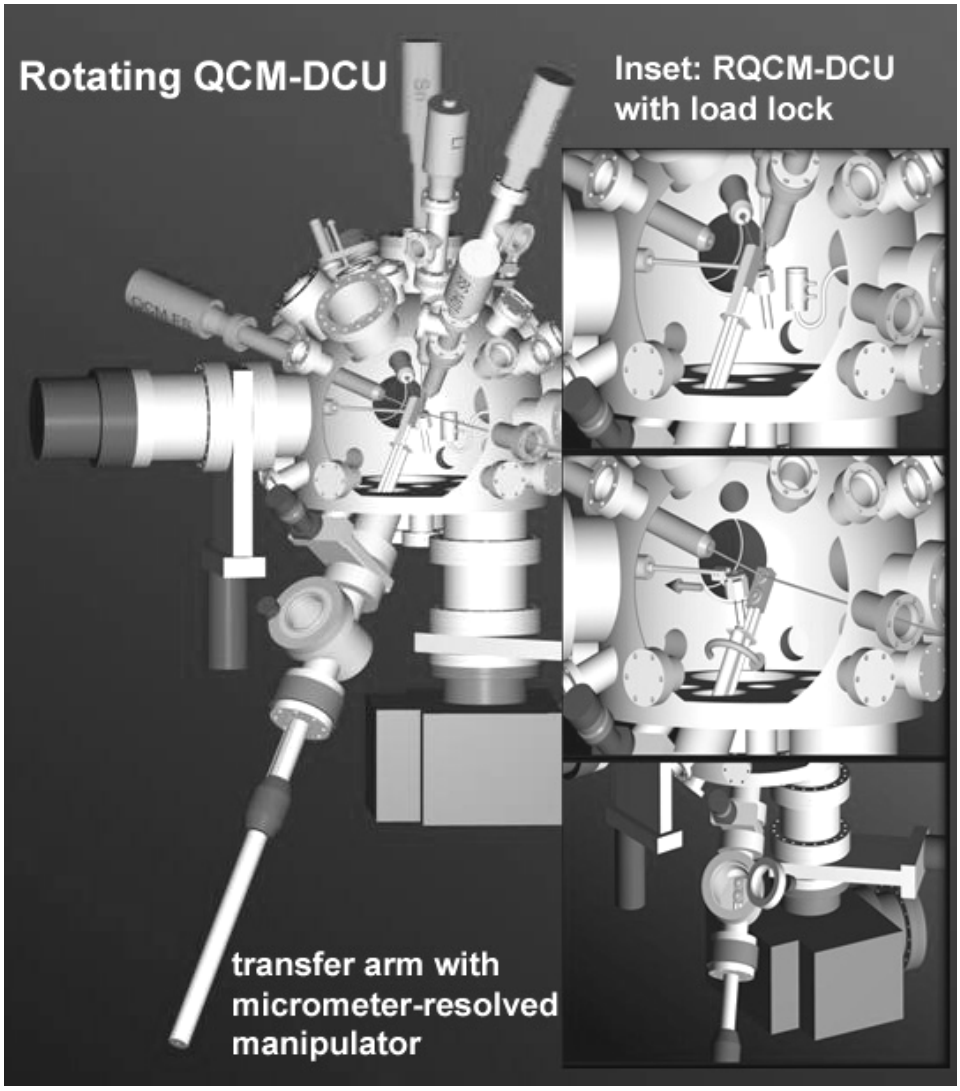

FIG. 13. Rotating QCM-DCU system in IMPACT.

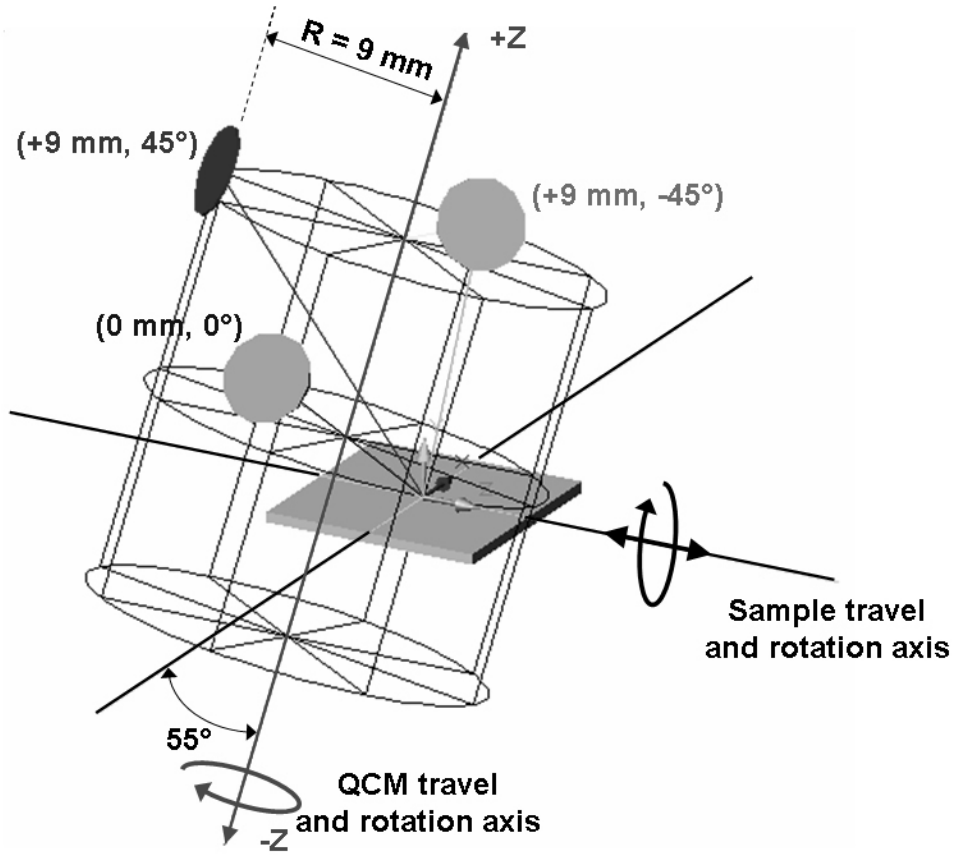

FIG. 14. Geometry of the rotating QCM system, showing three positions of the QCM that illustrate the sign convention for linear and angular displacement.

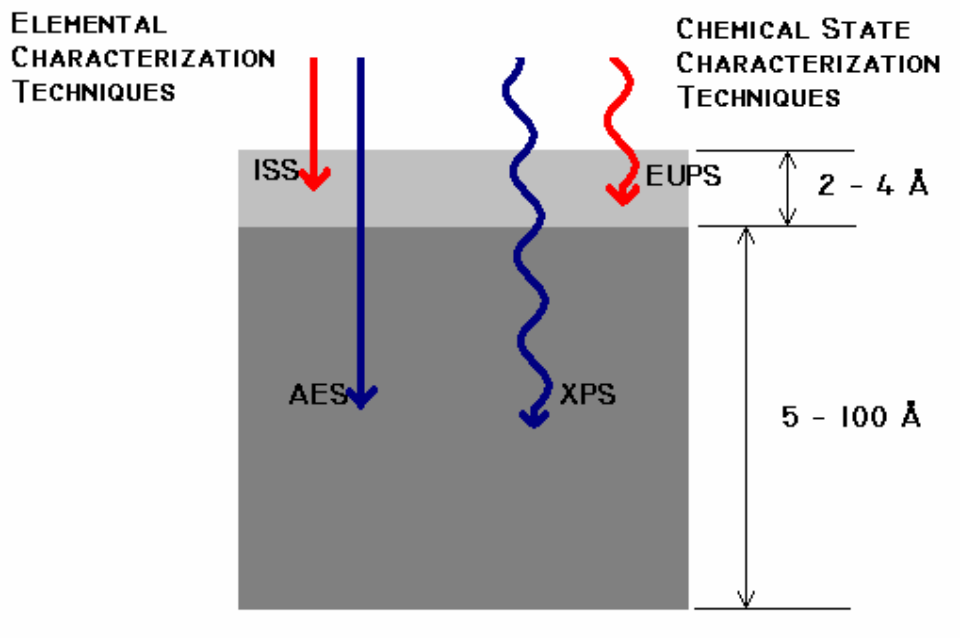

FIG. 15. Complementary surface characterization techniques in IMPACT probing two separate spatial scales at the surface.

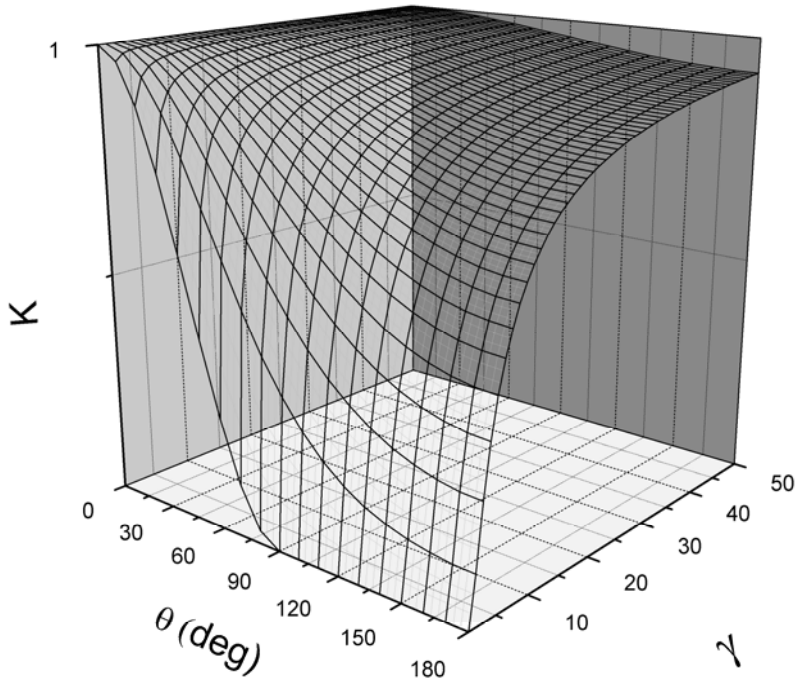

FIG. 16. Kinematic factor as a function of scattering angle and target-to-projectile mass ratio. Mass resolution increases by increasing the scattering angle and lowering the mass ratio.

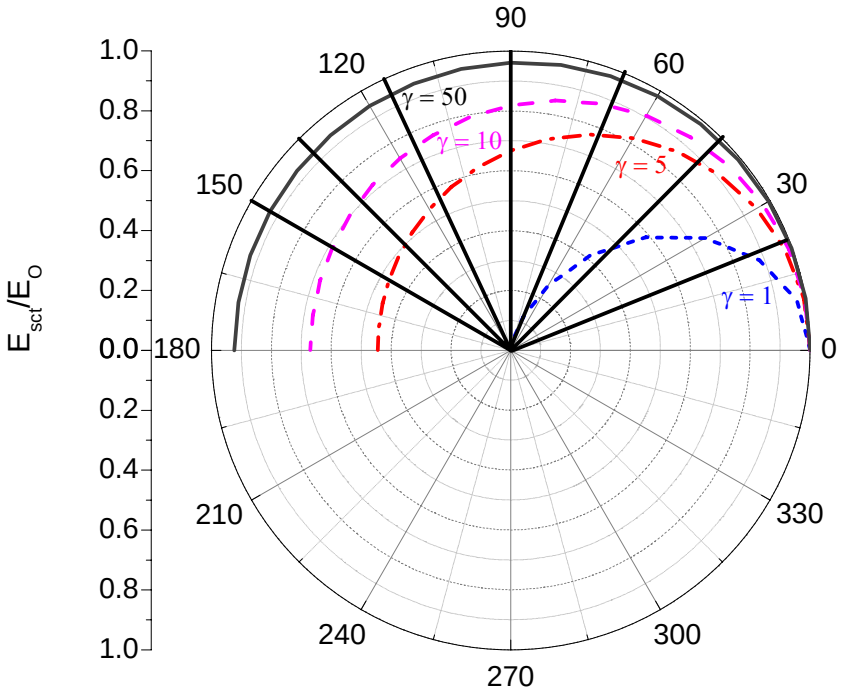

FIG. 17. Scattering kinematic circle showing the mass ratio and its dependence on the scattered angle in the laboratory frame.

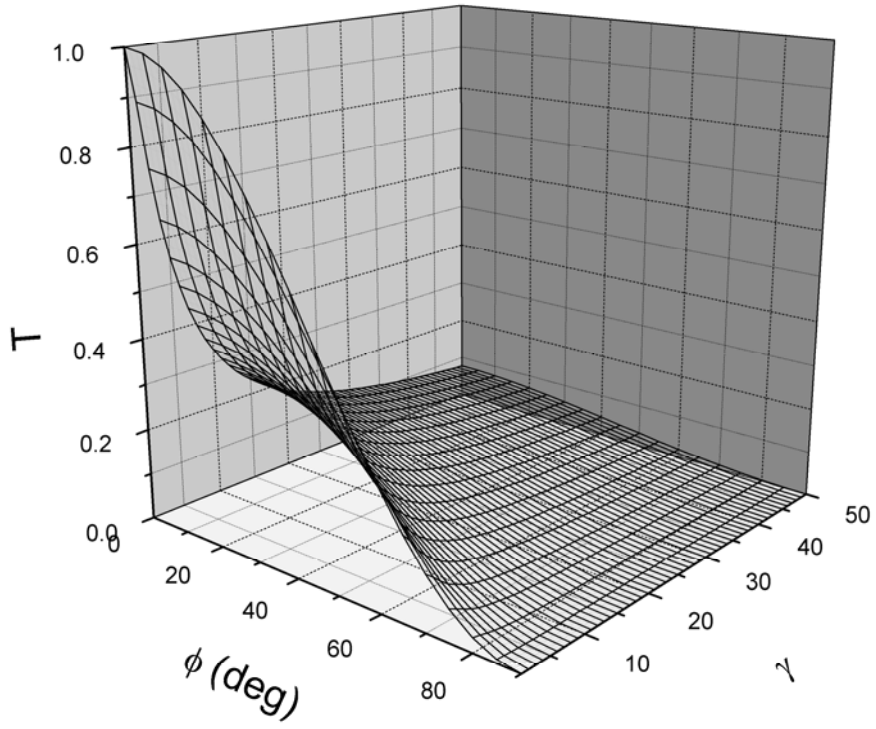

FIG. 18. Energy transfer factor as a function of mass ratio and recoiling angle.

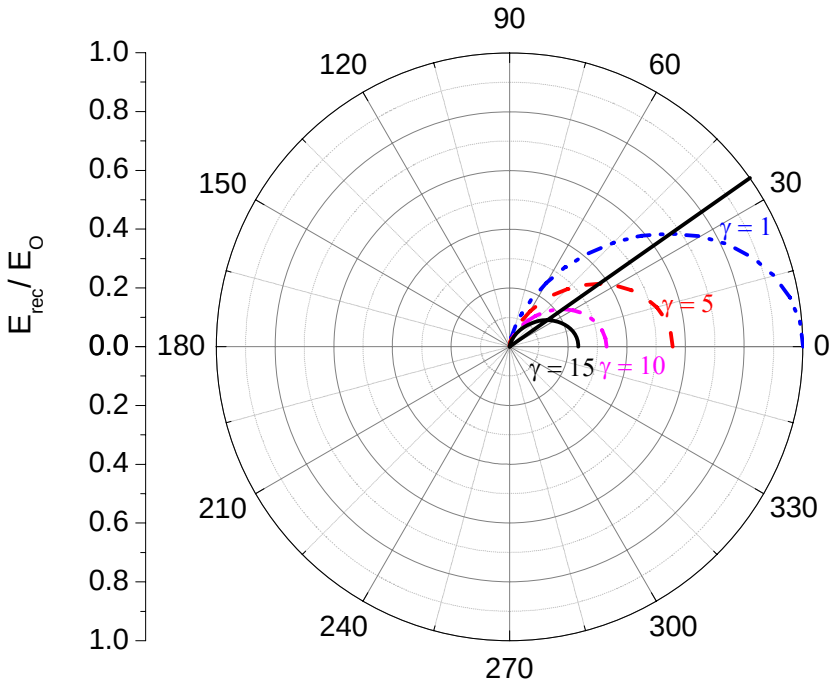

FIG. 19. Kinematic circle diagram for recoils with mass ratios and scattering angles relevant to recoil detection in the laboratory frame.

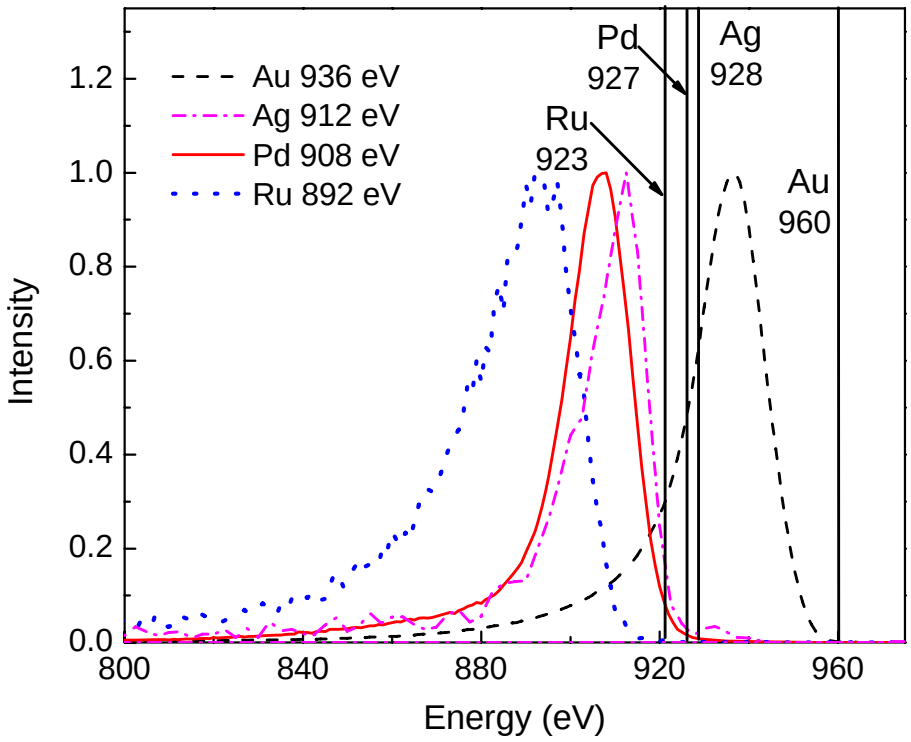

FIG. 20. ISS scans of different elements obtained by measuring the energy of 1 keV He ions scattered at 90° from the incident direction.

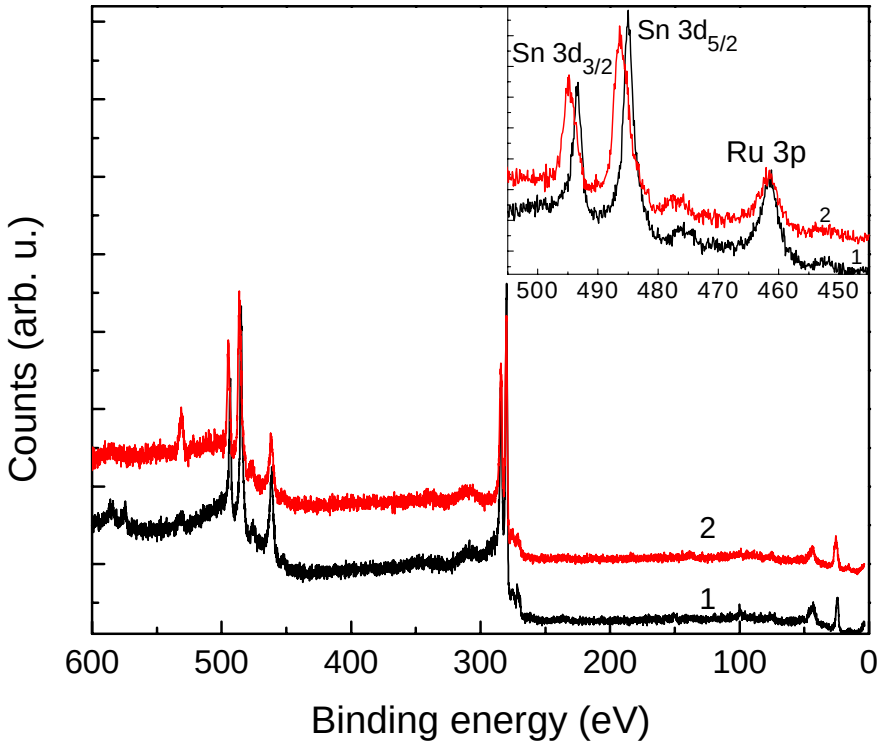

FIG. 21. XPS spectra obtained from Ru sample deposited with thermal Sn. Spectrum (1) recorded in situ with a Sn flux of 5×10^{16} cm^{-2}. Spectrum 2 is taken after exposing the sample to air, which led to oxidation. Inset shows the shift in Sn 3d photoelectron peaks due to oxidation.

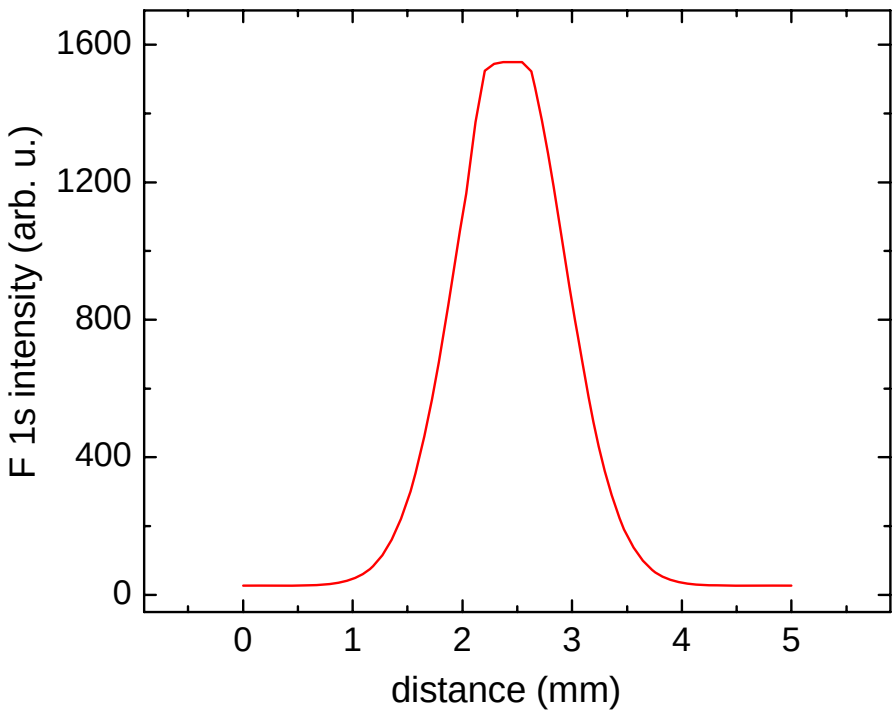

FIG. 22. XPS line scan across 1.3 mm wide Teflon sample. F 1s photoelectron peak at 689 eV is used.

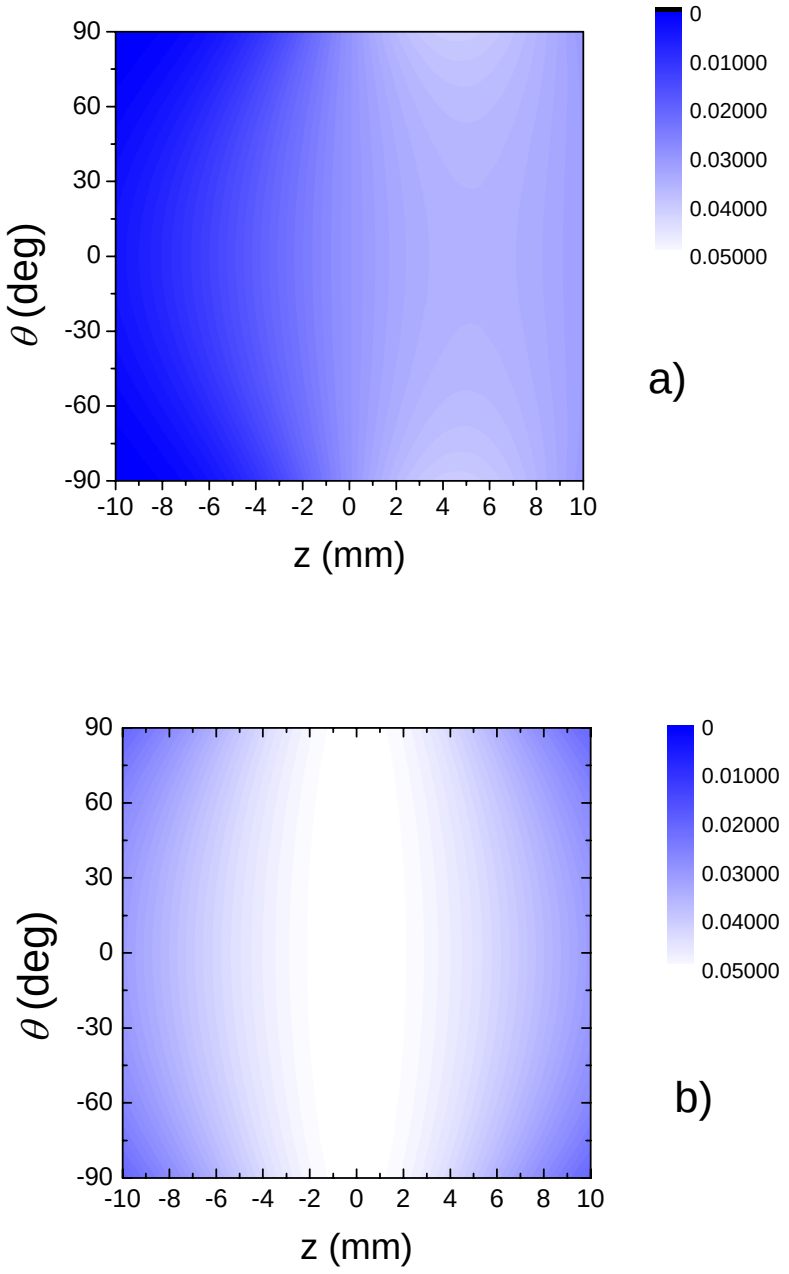

FIG. 23. Fraction of the sputtering flux with cosine distribution collected by the QCM crystal as a function of the cylindrical coordinates (z, θ). Two sample tilts are shown: a) 0° and b) 55°.

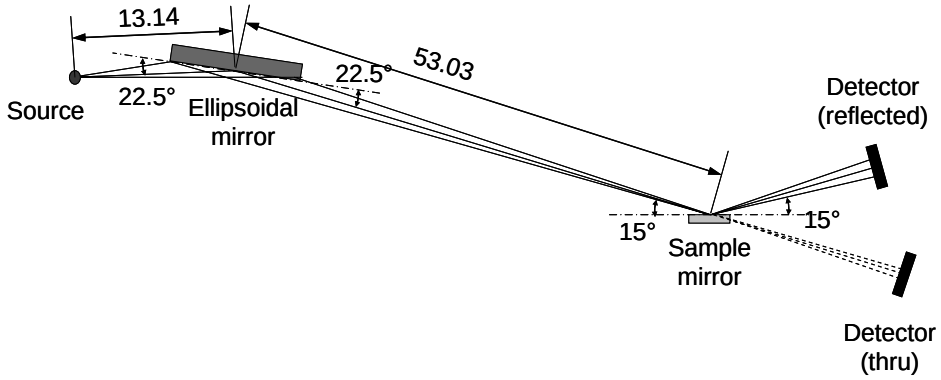

FIG. 24. Schematic of the reflectometer setup in IMPACT. Dashed lines indicate the path of the light when the sample is retracted. Distances are shown in cm.

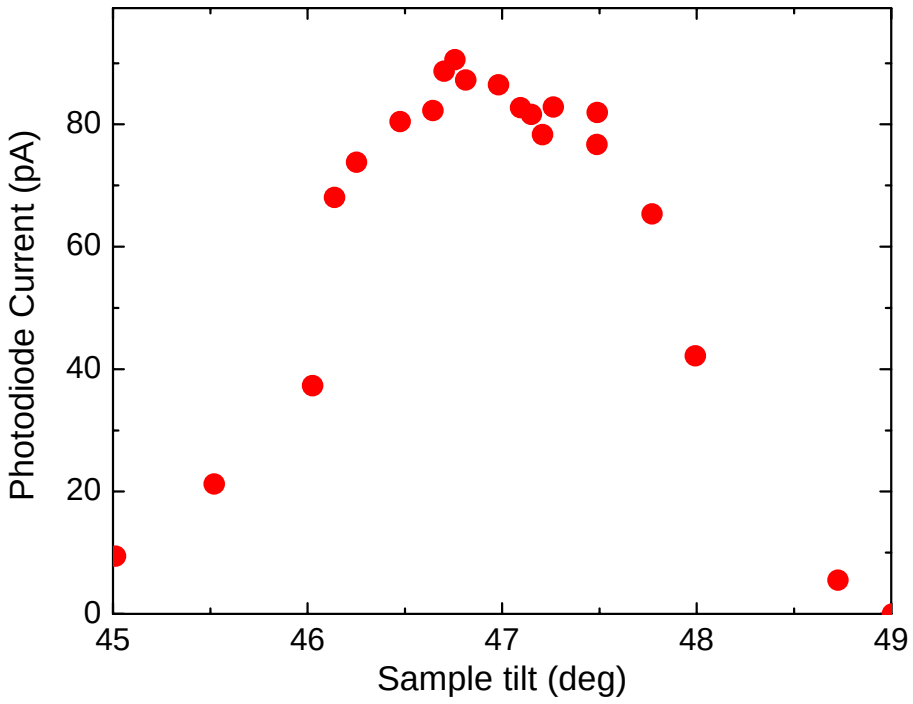

FIG. 25. Variation of photocurrent with the tilt of the sample. The flat top between 46.5° and 47.5° indicates that the spot on the photodiode is smaller than the active area of the detector.

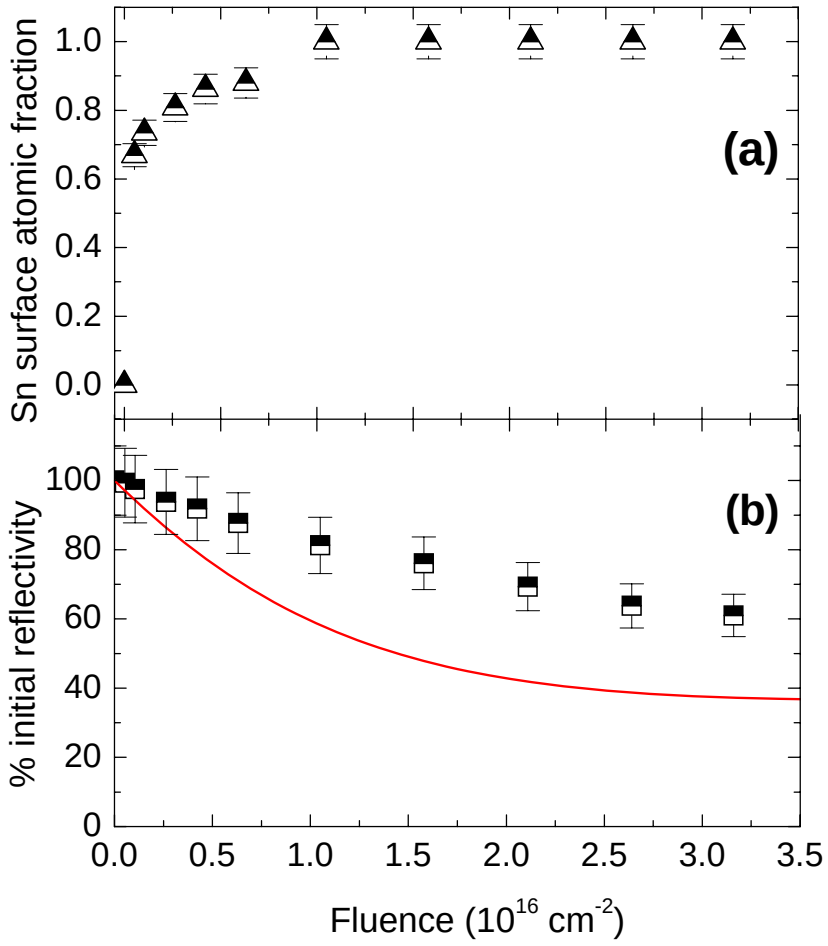

FIG. 26. Estimated surface Sn atomic fraction for various thermal Sn fluences (a). It shows Sn fraction reaching a steady state value of 90-100% coverage at a Sn fluence of about 10^{16} cm^{-2}. The effect on the relative 13.5-nm reflectivity during deposition is given in (b). The solid curve in (b) corresponds to IMD theoretical Fresnel reflectivity.

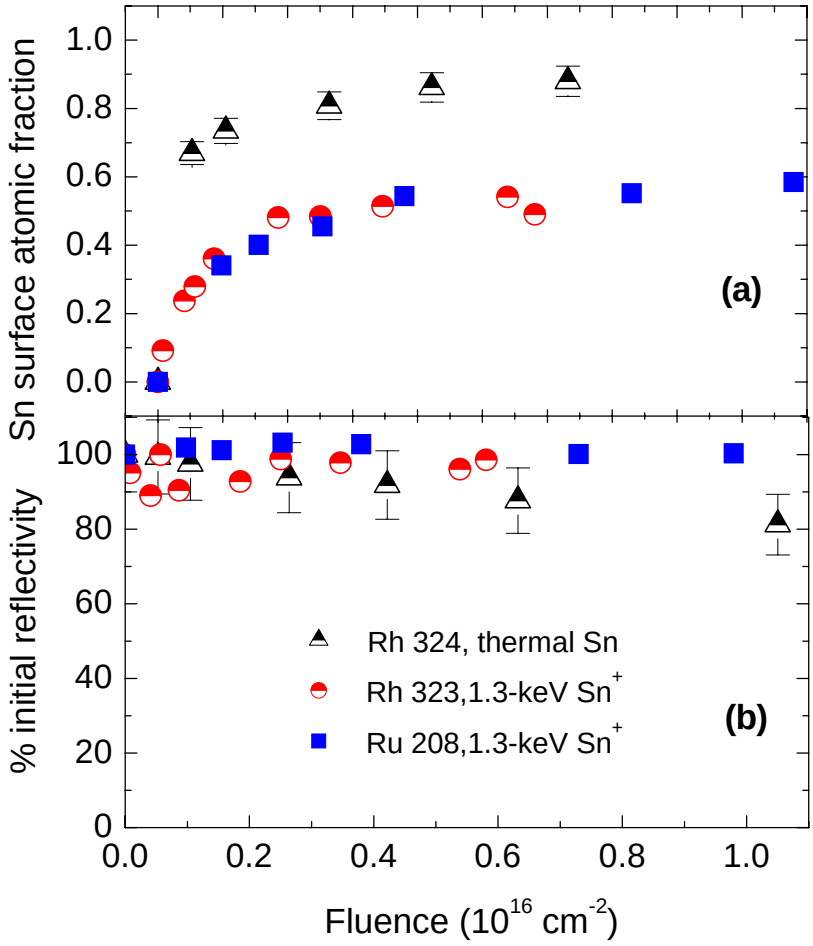

FIG. 27. Sn surface atomic fraction measured with LEISS (a) and the relative 13.5-nm EUV reflectivity loss measured with the EUVR for energetic and thermal Sn deposition (b).

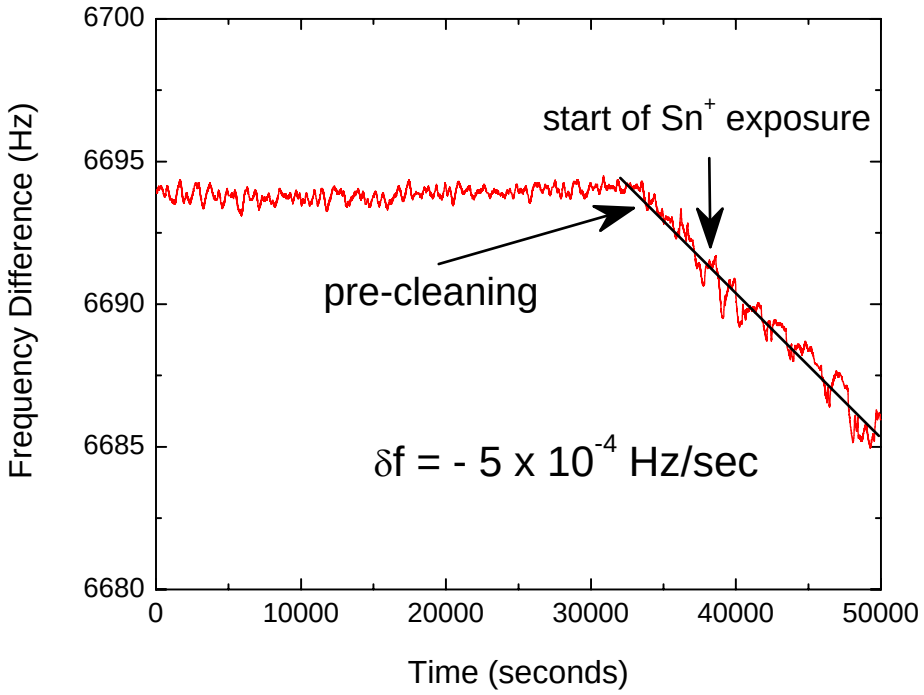

FIG. 28. Raw data of QUM-DCU showing the frequency variation as a function of time collected during Rh sample exposure to 1.3 keV Sn ions.